MASTER THESIS

TOWARDS THE DESIGN OF A VIBRATION MONITORING SYSTEM FOR A ROTOR BLADE SYSTEM IN OPERATION

AN EXPERIMENTAL INVESTIGATION

M.C. Madhar

FACULTY OF ENGINEERING TECHNOLOGY

CHAIR OF DYNAMICS BASED MAINTENANCE

Document Number:
CTW.16/TM-5784

NOVEMBER 28^{th}, 2016

UNIVERSITY OF TWENTE.

MASTER THESIS

Towards the design of a vibration monitoring system for a rotor blade system in operation

An experimental investigation

by

Mohammad Chefiek Madhar

Date:
November 28^{th}, 2016

Supervisors:

Andrea Sanchez Ramirez MSc.
UNIVERSITY OF TWENTE
Faculty of Engineering
Technology Chair of Dynamics Based Maintenance

dr.ir. Richard Loendersloot
UNIVERSITY OF TWENTE
Faculty of Engineering Technology
Technology Chair of Dynamics Based Maintenance

prof.dr.ir. Tiedo Tinga
UNIVERSITY OF TWENTE
Faculty of Engineering Technology
Professor Dynamics Based Maintenance

Acknowledgement

This report is the result of my research at the chair of Dynamic Based Maintenance for the Master Degree in Mechanical Engineering at the University of Twente. Initially, I was enrolled at the department of Mechanical Automation & Mechatronics, but as the field of vibration monitoring and its applications peaked my interest, I decided to do my final project at DBM.
This thesis would not have been possible without the help of a number of people. First of all I would like to thank Andrea for her supervision throughout the project. She made it top priority to be always available for discussions and provided the necessary help when needed. I am very grateful for that. Your unique approach at the start, for tackling the whole research is something that I will definitely take with me. Furthermore I would like to thank Richard Loendersloot for his critical comments and the insightful advices for approaching some of the challenges in this project. Also a special thanks to Tiedo Tinga for his comments and for allowing me to do my thesis at this department. Then of course special gratitude to Ronald Aarts for granting me the freedom to do the project outside the Automation department and for all the discussions we had over the past years. I am also grateful to Norbert and Axel for all their help and the experiences I gained in the workshop and laboratory for completing my setup. Furthermore to my fellow colleagues from the 'MS3Bazen' room I would like to apologize for not contributing anymore to the puzzles due to its "increasing difficulty". But I enjoyed our time in the room and I wish you all the best.

I started my adventures here at the University with my Surinamese group, Annemieke, Cyrano, Ignaas, Jina, Nelson, Roswita and Satish. Our support towards each other was admirable. Together with the new friends we made here, we had unforgettable moments. I will forever cherish these memories as we were the starting few of many more from our country to enroll at this university.
With that being said, my stay here in the Netherlands would not have been possible without the support of my family in Suriname who allowed me to do my Master and supported me in this decision. My family here in the Netherlands, who I am grateful for the occasional recreational visits outside Enschede. Last, but certainly not the least, I would like to thank my awesome girlfriend, Madelon for being forced into this long distance relationship and still having the patience to hear about my difficulties during my study. Your support kept me going.

Now, towards the next challenges in life!

Enschede, November 2016
Chefiek Madhar

Summary

In order for critical mechanical systems to maintain its functionality, their condition must be periodically evaluated to decide upon the required maintenance activities to be performed. Vibration monitoring is recognized as a valuable tool for providing information about the current state of the component. Developments of integrated sensors, embedded processing and wireless communication provide possibilities for on-blade monitoring, where the actual loading is taking place. However, obtained vibration signals can be decomposed in many different ways. Finding the parameters that actually describe the system and defining their critical values that indicate a substantial amount of damage are not trivial problems.

This research then contributes to the experimental investigations of vibrations in a rotor blade system by means of a demonstrator. The investigations were done for the forward flight case of the helicopter. With this flight condition the helicopter rotor blades are exposed to a cyclic changing loading of the airflow. Phenomenas found in rotating blades will then be different due to this non-axisymmetric airflow. Most interesting phenomenas to explore were the influences of lagging moments on blade flapping, the dissymmetry of lift and finally the harmonic response of flexible blades during forward flight.

The demonstrator consists of a hanging, non-rotating blade that allows flapping, lagging and pitching motions. The phenomenas in the forward flight were translated into appropriate requirements and measurement strategies for the RBS demonstrator to represent these effects.
The experiments on the demonstrator showed how sensitive the blade reacted to a series of different excitations, therefore proving that vibration monitoring on the rotor blade is a complex task for the different phenomena encountered in forward flight. From the measurements, it could be seen that lagging influences the flapping motion by reducing its baseline frequency amplitude and increasing harmonics in the blade. With these higher harmonics less rigid behavior is found in the blade's motion, leaving the blade more vulnerable to aeroelastic effects.
As rotor blade coning can be seen as variation of the rotational stiffness in the blade's hinges, this determines the stiffness distribution throughout the blade. Cyclic changes of the loading in forward flight can result in variations of this stiffness distribution. In the demonstrator this was represented with three different torsion springs in the blade's hinges. The analyses showed then that when the blade had a structural mode at a harmonic of the excitation frequency, the blade responses at that frequency amplified. The eigenfrequencies of a rotating blade are a combination of structural properties and stress stiffening effects. The influences of lagging on flapping in the demonstrator showed then that the flapping modes can shift. As damage was introduced in the system, reduction of the baseline excitations in the response could be seen with an increase of higher frequency vibrations. Due to the sensitivity of the system to higher harmonics, a clear boundary between the operations of the pristine and damaged blade was hard to realize. Therefore future investigations should account for these occurrences, so that further analyses is possible to find the deviations in operations between these two cases.

Contents

Nomenclature

Abbreviations

DOF	Degree of Freedom
EMA	Experimental Modal Analysis
FBS	Function Behavior Structure
HD	Harmonic Distorted
HUMS	Health and Usage Monitoring System
MSE-DI	Modal Strain Energy Damage Index
ODS	Operating Deflection Shape
OMA	Operational Modal Analysis
RBS	Rotating Blade System
RTB	Rotor Track and Balance system
SHM	Structural Health and Monitoring
TS	Torsion Spring

Greek Symbols

α	Angle of attack	[rad]
η	Leading/lagging angle	[rad]
Ω	Rotational speed	[rad/s]
Φ	Induced flow angle	[rad]
θ	Pitch, feathering angle	[rad]
θ_0	Collective pitch angle	[rad]
Ψ	Azimuth angle	[rad]

List of symbols

F	Force	[N]
f_{fr}	Rigid lagging frequency	[Hz]
$f_{f\,el}$	Elastic flapping frequency	[Hz]

f_{lr}	Rigid lagging frequency	[Hz]
M_F	External force moment about flap axis	$\mathrm{N} \cdot \mathrm{m}$
M_L	External force moment about lag axis	$\mathrm{N} \cdot \mathrm{m}$
p	Pressure	Pa
U_P	Inflow velocity perpendicular to rotor plane	[m/s]
U_T	Inflow velocity tangential to rotor plane	m/s
V	Forward velocity	[m/s]
V_c	Rate of climb	$[m/s]$
x	Blade feather axis	$[-]$
y	Blade flap axis	$[-]$
z	Blade lag axis	$[-]$
c	Rotational stiffness	$[\mathrm{N} \cdot \mathrm{m/rad}]$
D	Drag	[m/s]
K	linear stiffness	[N/m]
L	Lift	[N]
U	Relative inflow velocity	[m/s]

Chapter 1

Introduction

In order for critical mechanical systems to maintain its functionality, their condition must be periodically evaluated to decide upon the required maintenance activities to be performed. Vibration monitoring is recognized as a valuable tool for providing information about the current state of the component. However, the obtained vibration signals can be decomposed in many different ways. Finding the parameters that actually describe the system and defining their critical values that indicate a substantial amount of damage are not trivial problems.

A traditional approach to solve these questions is the so called data-driven approach, where historical measurements are correlated with damage patterns in the system. In this way is recognized which are the most significant features and their values for the most common failures observed. An inherent problem to this approach is the need of data, therefore such an approach cannot be applied to components which have not been monitored yet. This is the case for rotating blades as found in helicopter rotors. Although rotor vibration is known as a main source of vibration in helicopters, the monitoring of the blades motion was limited due to connectivity issues.

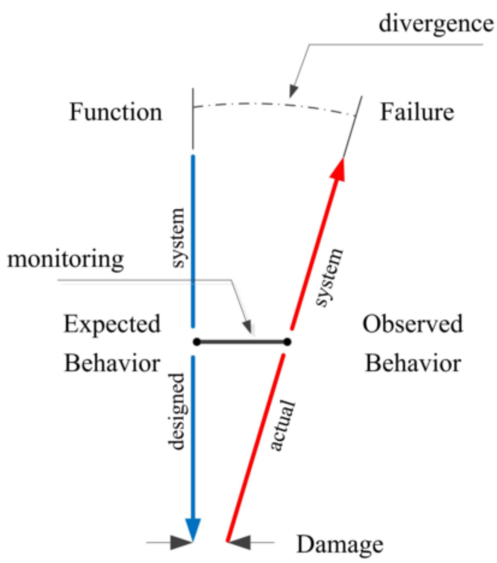

Figure 1.1: Behavior divergence scheme [17]

A solution for monitoring of rotating blades has arisen with new developments in integrated sensors, embedded processing and wireless communication. These technologies allow the evaluation of vibration signals in situ and the transference of data from the key parameters, wireless to a fixed station. These

enable a wider range of load and condition parameters to be monitored and the analysis of all collected data feasible. Yet the problem to know what to measure remains.
As an alternative to the data-based approach, a physics based approached is seen as a valuable option. This is one of the main research focus of the chair of Dynamics Based Maintenance (DBM), which promotes the understanding of the physical phenomena of the failure behavior as basis of maintenance and monitoring activities. This is exemplified in the research on designing vibration monitoring system as carried out by Sanchez. She states that prior to the design of the monitoring system, the monitored system must be understood. Here it is referred not only to the designed system, but also to the divergence between the expected behavior and the observed behavior of a system for which material damage may lead to system failure. The situation is depicted in figure 1.1.

1.1 Motivation for on-blade sensing

In a helicopter the Health and Usage monitoring system (HUMS) is responsible for collecting operational data of the vehicle to monitor safety, usage and maintenance parameters. Vibration data was initially used for performing adjustments by the rotor track and balance system (RTB) to minimize rotor vibrations resulting from unbalances due to non-uniformities between the blades and/or the dissymmetry of the rotor in forward flight [2].
Most HUMS address vibrations on the fuselage, given the assumption that rotor fault effects are transferred to the frame. The initial thought was that existing RTB techniques could just simply be extended to identify the faults. If the mistracking cannot be corrected by balancing, then damage may be indicated. Recent research revealed however that the RTB adjustments may mask faults rather than indicate their presence. The data is only used for compensation of unwanted vibrations, therefore the underlying cause of the vibrations is left undetermined. Extending the capabilities of the HUMS to rotor fault detection is therefore a necessity.

1.1.1 Integrating rotor health monitoring in HUMS

Rotor health monitoring needs to provide information about significant damage which occurs on the rotor blade. New developments of the HUMS should include the ability to extract the signs of beginning failure from the collected data. As the loading on the helicopter blades varies considerably with flight condition any successful rotor HUMS would have to distinguish rotor damage-induced effects on its input data from a naturally wide variation of influences due to operation, usage and/or age. Pawar and Ganguli [12] discuss two technical approaches to rotor health monitoring:

1. Monitoring hub loads and fuselage for transmitted effects of damage in one blade. Generally for each revolution of the rotor, each blade transmits a periodic loading on to the rotor hub. If a blade is then damaged, these periodic effects will vary significantly and other harmonics might occur. These phenomena can be used as suitable damage indicators. Ideally, experimental data could be used to study the effect of damage on the blade and rotor system behavior.

2. Monitoring of an isolated rotor blade where any change in its behavior compared to an undamaged blade can be used as a damage indicator. (Tip flap, lag and torsion displacements, strains along the length of the blade, loads or acceleration, natural frequencies, mode shapes, modal curvatures and other non-destructive tests).

In the first approach vibration data on the fuselage is used as the primary input to rotor HUMS. However, new developments in helicopters may make realizing a fully robust technique for damage detection to become more difficult due to data contamination. Composites are increasingly used in fuselage elements, which provide increased levels of structural damping. Measured vibrations on the fuselage might have poor signal to noise ratios resulting in inaccurate or no damage detectability. Another development to consider is

active and passive rotor vibration suppression systems in modern helicopters. These complicate the actual vibrational transferences on the fuselage, making detection of fault signatures from background vibrations harder to distinguish. More advanced signal processing algorithms will be required.
Given the difficulties in rotor damage detection that arise from new helicopter developments, the second approach might prove to be a more suitable solution. Emergent technology such as integration of embedded sensors and increased processing power enables the possibility of measuring parameters on the blade, where the actual loading is taking place. Contamination of vibration data by the fuselage can then be eliminated and more accurate detection methods can be developed. The occurrence of aero-elastic problems in the blade can also be analysed more effectively as more certainty is obtained in the vibration data.

1.1.2 Fault detection strategy for on-blade monitoring

On-blade monitoring through the HUMS relies on machine-learning techniques which can be categorized into supervised and unsupervised approaches. The supervised approach allows the machine to identify signatures in the data that correspond to pre-specified faults. A database of known faults will have to be established (mathematically or experimentally) prior to the identification. The unsupervised approach reports anomalies when deviation from the expected condition of the system is detected. The machine will have to be closely familiar with a wide variety of normal operating behavior.

A series of strategies for fault detection investigations has already been set and research on each of these topics contribute to the realization of an effective rotor HUMS [3]. Near term development in HUMS emphasizes on unsupervised techniques as this can already be applicable to existing HUMS data. For certain rotor faults there are already detectable changes in some of the vibration measurements being recorded on most HUMS, but absents the thresholds to alert faults.

The possibilities for fault detection using unsupervised learning could most easily be implemented by applying anomaly detection techniques to available vibration data. From the data, anomaly models could be developed and evaluated using multiple rotor measurements (e.g. different vibration harmonics, multiple flight states) to describe the behavior of the rotor data in undamaged conditions. It will be necessary to select a subset of the available measurements to incorporate into the models, and determine what pre-processing to apply. This would best be achieved by considering, from a theoretical basis, which measurements are most likely to indicate that a fault is present. The fault detection will require analysis of data from several different operating conditions, as well as careful consideration of any maintenance inputs. Once the rotor data has been modelled, fault case data could be used to determine which faults may be detected by comparison with the model. This fault data can results from known fault histories or estimated from theoretical modelling of faults.
The approach as described above can result in a clearer assessment of the feasibility of rotor fault detection in the HUMS especially for establishing which faults are detectable and most likely not detectable.

This thesis contributes to the design of a vibration monitoring system for rotating blades. The direct monitoring of blades behavior is expected to provide valuable information not only on assessing the damage of these structures, but on the performance of the system they belong to, i.e, helicopter, wind turbines. Within the chair of Dynamics Based Maintenance, there has already been an important body of research carried out in damage characterizations of beam structures and helicopter blade monitoring. This will be discussed in the next section.

1.2 Related research at the DBM

The topic of damage characterization on beam-like structures has been object of Structural Health Monitoting (SHM) research within the DBM chair. In his PhD, Ooijevaar [10] developed guidelines for detection, localization and characterization of damage in composite skin-stiffener structures based on changes in the dynamic behavior. He stated that mode shape curvatures combined with the modal strain energy damage index (MSE-DI) algorithm were potentially powerful damage features and classifiers for the identification of damage in several advanced composite skin-stiffener structures. From his work could be concluded that a vibration based damage identification strategy should be tailored to the system and requires thorough physical understanding of the potential failure mechanisms, the critical damage locations and their effect on the dynamic behavior.

Teunis [22] experimentally introduced structural health monitoring technology on a composite beam for a clamped and hinged configuration at its end. The beam was then excited, allowing to perform flapping motions. Through Experimental Modal Analysis (EMA) and Operational Modal Analysis (OMA) techniques mode shapes were extracted for obtaining the MC-DI and MSE-DI. For single damage scenarios it was possible to detect damage if a threshold peak value was set. It was also possible to localize the damage within a certain distance and determine accumulating severity. Furthermore, in the multiple damage scenarios it is more difficult to determine the damage locations with confidence.

1.2.1 Dynamic behavior characterization

Previous two mentioned researchers evaluated the feasibility of vibration-based SHM techniques to beam-like structures. The implications of operational condition for the evaluation of such structures with the proposed methods was however not considered. Another research line with the DBM considers the functionality of the monitored system as staring point of the discussion on methods to use. For this end, the design methodology Function-Behavior-Structure (FBS) is used.

Oosterik [11] used this FBS structure to decompose the complexity of a helicopter into key features of its dynamic behavior that can be used for monitoring purposes. The functionality of the helicopter was then classified as follows:

1. Generate vertical lifting force (thrust) in opposition to the helicopter weight.

2. Generate a horizontal propulsive force for forward flight.

3. Generate forces and moments to control the altitude and position of the helicopter in three-dimensional space.

These functionalities are related to specific operational states of the helicopter (figure 1.2). The added value of a physics based functional model was also demonstrated, where the expected behavior before and after damage of the structure was constructed. After comparison with the actual behavior, effects due to damage and operation could be distinguished.
The work of Oosterik focused on hovering flight, for which rotation and aerodynamics already cause complex coupling phenomena between the different degrees of freedom of the blade. He could numerically demonstrate the use of modal strain based methods for the identification of damage in the blades. However for non-stationary loading as experienced during forward flight, the influence of non-linearity effects would make the characterization of the modal properties of the blade more difficult.

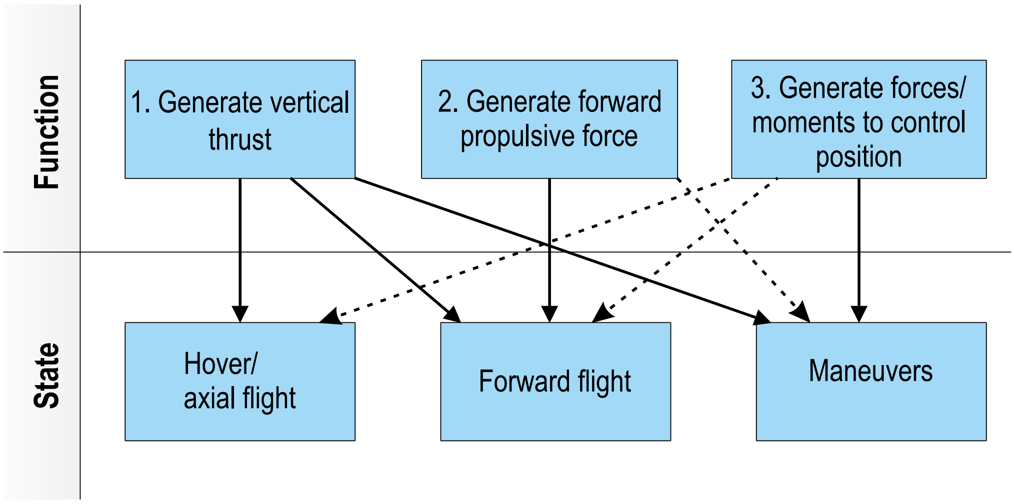

Figure 1.2: Relation functionality and operational state (adapted from [11]).

1.2.2 First approach to a RBS demonstrator

A first approach to enable the experimental work on beam structures in rotating-like conditions was started by Wolters [25], who designed a demonstrator of the behavior of a Rotor Blade System (RBS) for on-blade monitoring. His design was based on achieving a stiffness distribution similar to an actual helicopter blade. To this end, the demonstrator enabled 3 degrees of freedom of which pitching and flapping could be excited simultaneously through actuators. The lagging motion was set free. Furthermore the similarity with the ratio of the rigid body modes to the elastic modes was achieved by introducing rotational stiffnesses in the flapping and lagging hinges. The demonstrator was build modular so that different blade profiles could be tested as well as different torsion springs to vary the elastic behavior.
This demonstrator showed however, some problems that were in general caused by a disturbed transference of the loading from the exciters to the test beam. Furthermore it did not display any coupled effects as those highlighted in Oosterik's work.

1.3 Assignment objective

This thesis is a continuation of the summarized work in the previous section. The research intends to bridge the paths of assessing a structure's health while considering its functional role in a mechanical system. This is possible by understanding the most significant dynamic features of the blade during operational conditions with cyclic loading as encountered during forward flight. This work then intends to contribute to the development of on-blade vibration monitoring systems. The research question can therefore be formulated as follows:

- *How can the blade responses to cyclic loading of the environment be represented in the existing demonstrator?*

In order to obtain an experimental setup that would allow to explore the behavior of the blades during forward flight, the existing demonstrator needs to be re-designed and the input excitations customized to the condition. Answer to this question should lead to reducing the uncertainties as a consequence of the operational behavior and damage behavior in vibration monitoring. Therefore a conclusion about the boundaries of the grey area in figure 1.3 should be achievable.

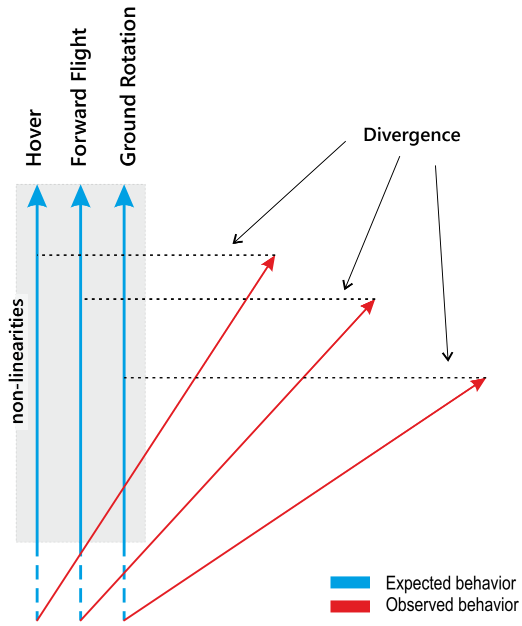

Figure 1.3: Grey boundary in behavior divergence scheme.

1.4 Thesis outline

The first part of the thesis, chapters 2 and 3, deal with the re-design of the demonstrator according to the requirements for representing particular operational conditions during forward flight. Two main aspects were considered. The existence of coupled modes due to Coriolis coupling, and the effect of flexible boundary conditions that allow the existence of rigid body and flexible modes.

The second part, chapter 4 and 5, involves the experimental investigations where the operations of the demonstrator is first verified. Subsequently chapter 5, corresponds to the characterization of the blade response against the harmonic environment i.e. the cyclic loading environment. The functionality of the blade is evaluated when a controlled input is given for reducing the dissymmetry of lift.

The thesis is then completed with conclusions of the performed experiments and recommendations for further analyses for vibration monitoring with the demonstrator.

Chapter 2

Rotor Blade Systems (RBS)

Rotating blades are key components of many mechanical systems due to their ability to either supply or extract power from a fluid. The former is the case of helicopters, whose blades use rotation to create lift. By changing the angle of attack of the blade, vertical and horizontal motions of the rotorcraft are possible. The case of constant loading conditions, as occurring in hovering, has already been discussed in previous research. However, the transition towards a forward flight configuration introduces additional phenomena that need to be understood. To assign the forward flight behavior then on to the RBS demonstrator, knowledge of the basic operating principles and relations with forward flight is presented in this chapter.

2.1 Operating principles

In the fully articulated rotor system each blade is attached to a series of hinges which are connected to the rotor hub. The hinges enable independent movement usually in 3 directions i.e. flapping, forward and pitching directions as shown in figure 2.1. Compared to fixed-winged aircraft, helicopter blades need more power, have to withstand higher stresses, are harder to understand and control and have more complex stiffness distribution because of the rotation of the blades. It is therefore important to understand the aerodynamic environment and the loads affecting the dynamic response of the blades. As lift and drag play an important role in this, these will be discussed first.

2.1.1 Blade lift and drag

A helicopter rotor system generates lift, because the rotor causes a downwash of air, resulting in the helicopter being pushed upwards. A closer inspection of this process requires investigation of an airfoil. An airfoil can be defined as any surface designed to generate aerodynamic force when it interacts with a

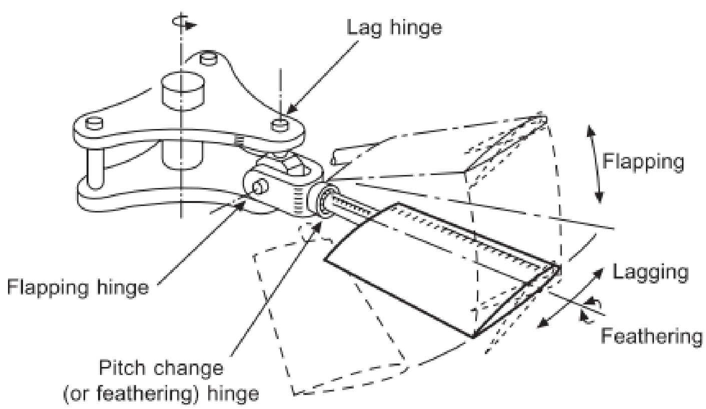

Figure 2.1: The articulated rotor blade system [1].

moving stream of air. Lift is the perpendicular component of a force that is exerted on a body moving through a fluid and drag is the force generated parallel and in opposition to the direction of travel. Drag is thus an unavoidable consequence of that movement.
Due to rotation of the rotor, the blades have an airspeed, either where the airfoil moves through the air or where the air moves past the airfoil. The resultant lift or thrust is the reaction to acceleration of a mass of air by the rotor blades. If enough power is applied to accelerate the air mass, the helicopter will fly.

To be able to characterize the loading on the blade, it is important to know the relative velocity and the direction from which the air appears to be approaching the airfoil. If the airfoil is slightly inclined to this direction, it changes the direction of the airflow and therefore the velocity resulting in acceleration and producing lift. The angle of the blade in this situation is also known as the angle of attack (AoA). In figure 2.2 can be seen that lift occurs perpendicular to the direction of relative airflow and that induced drag is measured along the direction of the airflow. The drag of a hovering helicopter is mainly induced drag that occurs while the blades are producing lift. There is also some profile drag on the blades, whose surface areas causes the air to resist movement. At (high) forward speeds, the profile drag will be larger than the induced drag. In this research both types will be considered 'drag'.

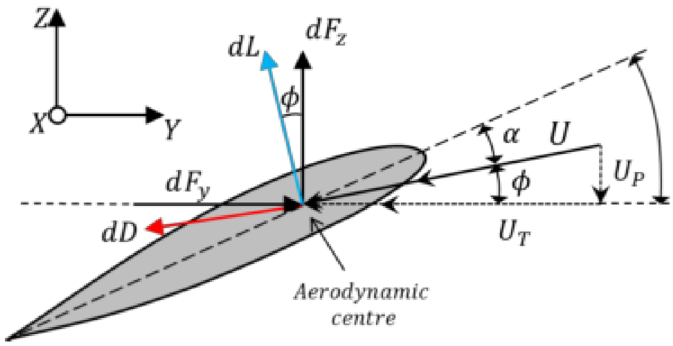

Figure 2.2: The blade element [11].

It is clear that helicopters can control lift by increasing or decreasing the angle of attack, resulting in either an increased or decreased change of velocity of the relative airflow. In earlier stages of the helicopter the amount of lift was controlled by just adjusting the rotor speed. Due to reasons of engine efficiency, swash-plates were introduced to allow adjustments in AoA while maintaining constant rotor speed. The swash plate consists of a stationary plate and a rotating part. The stationary part can be controlled by the pilot and the motion is passed on using a ball-joint. Changing then the AoA is done by letting the swash plate rotate the blade about its radial axis, which is known as feathering or changing pitch angles (indicated with θ in figure 2.2).
The way the pitch angles are changed can be done in a collective and cyclic manner. The helicopter uses this collective and cyclic pitch control to perform its motion in the air. Collective pitch control varies the pitch angle for all the blades by the same amount, thereby varying the magnitude of rotor thrust in vertical direction. In this way the helicopter's up and down movements are controlled.
The cyclic pitch control varies the pitch angle of the blades harmonically during the course of one full rotation. This action causes the rotor disk to direct its thrust forward allowing forward movements of the helicopter.

2.1.2 Forward flight

It is clear that lift and drag result from the relative inflow velocity, which is experienced differently by the blade for hovering and for forward flight. This section discusses the main differences between the inflow scenarios for both cases.

In a hovering flight configuration, the helicopter is able to remain in a constant position above the ground. The lift and thrust produced by the rotor system act straight up and must equal the weight and drag of the helicopter which act straight down. In forward flight the helicopter generates a forward propulsive force by directing the rotor thrust forward. Part of the total rotor thrust is then used for forward movement and part for maintaining altitude. Forward flight is thus an extension of hover and requires a combination of functions 1 and 2 (and 3) in the function-state diagram of the helicopter (see figure 1.2).

The flow through a rotor will be assumed quasi-steady and incompressible. For the case of axial flight, figure 2.3 considers a cylindrical control surface surrounding a control volume with radius R_1. The rotor has a radius R. At the top of the slipstream of the rotor, the air velocity relative to the rotor is the rate of climb V_c and has a pressure p_∞. At the rotor, the airspeed is gradually increased to $V_c + v_i$ while the pressure jumps to $p + \Delta p$ as consequence of the rotor thrust T. The slipstream velocity continues to increase downstream of the rotor, reaching a value of $V_c + v_2$ and a radius of R_2 where the pressure is p_2. The slipstream velocity is higher than the undisturbed axial velocity V_c.

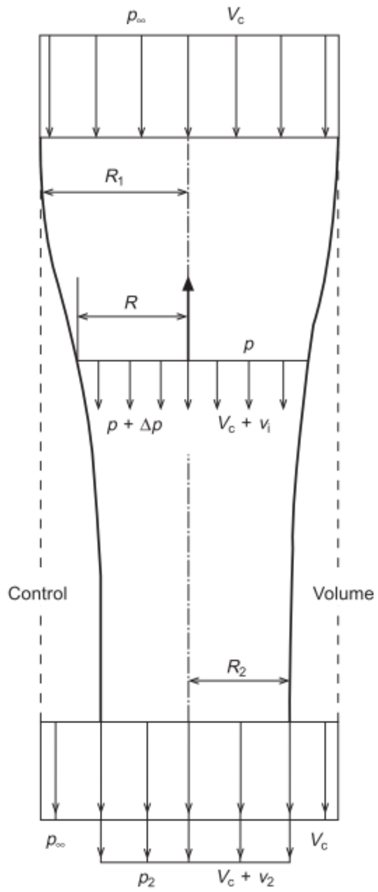

Figure 2.3: Rotor in axial flight [1]

In the case of forward flight, this axisymmetric flow through the rotor is lost. The rotor plane is tilted forward by using cyclic pitch. The total rotor thrust T is increased and also directed forward from the vertical. The resultant lift-thrust force can be resolved into two components: lift acting vertically upward and thrust acting horizontally in the direction of flight. In addition to lift and thrust, there is weight as the downward acting force, and drag as the rearward acting force.

The relative velocity of the air at the disk is now:

$$U = \sqrt{(V_{\infty} cos\alpha)^2 + (V_{\infty} sin\alpha + V_c)^2} \tag{2.1}$$

As the helicopter moves forward, it begins to lose altitude because of the lift that is lost as thrust is diverted forward. However, as the helicopter begins to accelerate, the rotor system becomes more efficient due to the increased airflow on the blades. The result is excess power over that which is required to hover. Continued acceleration causes an even larger increase in airflow through the rotor disc and more excess power.

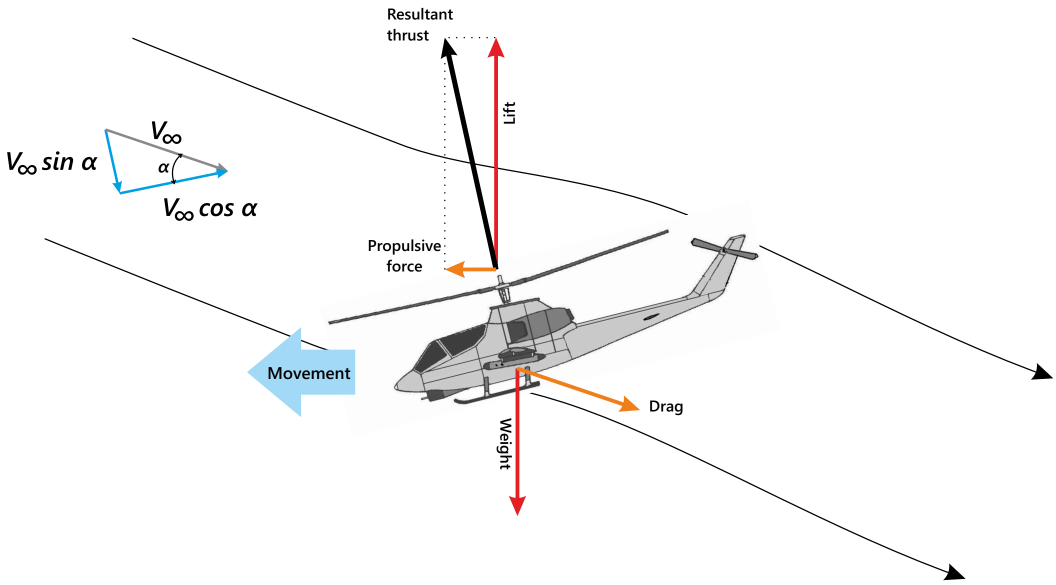

Figure 2.4: Forward flight by creating a forward propulsive force (adapted from [6]).

As the helicopter has a forward speed, the blade will experience a relative airflow dependent on the position of the blade at that moment in the rotation. This position on the rotor disk can be defined in terms of an azimuth angle Ψ. When the blade is pointing downstream, $\Psi = 0$ and for the blade pointing forwards, $\Psi = 180$.

Starting from the forward velocity V of the helicopter, the velocity vector can be decomposed in sideways, forwards, and upwards velocities:

$$V = \begin{Bmatrix} 0 \\ Vcos\alpha \\ -Vsin\alpha \end{Bmatrix} \tag{2.2}$$

The blade is rotating with angular velocity Ω. Now assume that the blade lies at an azimuth angle Ψ corresponding to an i,j,k axis as shown in figure 2.5. The $k - axis$ is pointing upwards. The velocity components on this blade can then be expressed in terms of Ψ. Additionally, rotation adds the Ωr component to the forward motion (j-component) of the blade. So the total velocity vector then becomes:

$$W_{ijk} = \begin{Bmatrix} -Vcos\alpha cos\Psi \\ Vcos\alpha sin\Psi + \Omega r \\ -Vsin\alpha \end{Bmatrix} \tag{2.3}$$

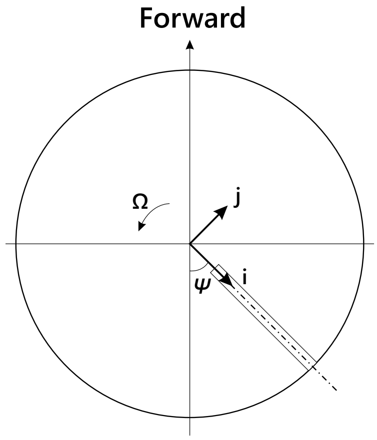

Figure 2.5: Blade axes in plane of rotor disk.

In undeflected position, the blade axes coincide with a reference frame at the center of the hub. When there is a flapping motion through angle β, a rotation matrix needs to be used to transform W_{ijk} to a xyz-frame:

$$[R]_{flap} = \begin{bmatrix} cos\beta & 0 & sin\beta \\ 0 & 1 & 0 \\ -sin\beta & 0 & cos\beta \end{bmatrix} \tag{2.4}$$

The velocity of the blade in forward flight as a function of the azimuth angle then becomes:

$$\begin{Bmatrix} -Vcos\alpha cos\Psi cos\beta - Vsin\alpha sin\beta \\ Vcos\alpha sin\Psi + \Omega r \\ Vcos\alpha cos\Psi sin\beta - Vsin\alpha cos\beta + r\dot{\beta} + v_i \end{Bmatrix} \tag{2.5}$$

Where contributions due to flapping, $r\dot{\beta}$ and relative wind due to induced velocity v_i have been added in the z-vector of the blade.

From above, the velocity component in x-direction can be neglected. The y and z velocity vectors correspond to the tangential and perpendicular components on the blade, U_T and U_P. For small values of β this becomes:

$$U_P = Vcos\alpha cos\Psi sin\beta - Vsin\alpha cos\beta + r\dot{\beta} + v_i \tag{2.6}$$

$$U_T = Vcos\alpha sin\Psi + \Omega r \tag{2.7}$$

The velocity components of the air relative to any point of the blade have been expressed in above equations and will be useful to understand how the blade is being excited in forward flight. The reader is referred to Bramwell [1] for more details.

2.2 Occurring phenomenas in rotating blades

The complexity of rotating blade systems lies also in certain phenomena occurring due to rotation and interaction with the environment. Adding to the fact that the helicopter blades are long and flexible, opens up more interactions between motion and environment. Flexibility of the blades is however required for forward flight, but also to increase flight comfort.
For hovering, converting torque in vertical thrust had effects on the rigid and flexible blade dynamics of the rotor system. These were in the form of blade coning, drag, Coriolis, aerodynamic coupling, stress stiffening, spin softening and aeroelasticity. Both the rigid and flexible behavior of the blade will act differently as consequence of the cyclic loading than in hovering. These will be discussed next.

2.2.1 Rigid blade behavior

The complete behavior of the rigid blade consists of a combination of coupled equations of motions due to Coriolis and aerodynamic damping. The Coriolis coupling is more of a structural coupling while the aerodynamic damping is expressed through the moments working on the blade from aerodynamic loading.

Coriolis coupling

Flapping of the blades in the rotating environment introduces the phenomenon called Coriolis, where an extra moment around the z-axis appears. This is known as the coupling between blade flapping and leading-lagging. Whenever there is a radial lengthening or shortening of the blade in a rotating frame of reference, Coriolis forces will appear. From the conservation of angular momentum equations this can be proven mathematically. For the case of pure flapping the following was derived by Oosterik [11] from a blade reference frame:

$$\sum M_x = 0 \tag{2.8}$$

$$\sum M_y = -I_{yy}\ddot{\beta} - \Omega^2[I_{yy}cos\beta + me_F x_g R^2]sin\beta \tag{2.9}$$

$$\sum M_z = -2I_{yy}\Omega\dot{\beta}sin\beta \tag{2.10}$$

From above equations can be seen that a moment around the z-axis appears (2.10) as a consequence of flapping in a rotating environment. This term is known as the Coriolis moment in the direction of rotation and causes periodic perturbation in the rotor torque if it is not released by a lag hinge.
Similar derivations can be done for the lagging motion when a lag hinge is present. This will however show that no extra moment in other directions will appear than in lagging direction. Coriolis coupling is thus a result of flapping in rotation.

Aerodynamic coupling

Hovering causes aerodynamic loading, which changes the dynamic behavior of the flapping and lagging motion. When deriving the aerodynamic moments for a blade for pure flapping and pure lagging, both the perpendicular and tangential velocity components become a function of flapping and lagging [11]. Using those loadings in the coupled equation of motion for flap/lag motions results in inhomogeneous and nonlinear differential equations.
The complete behavior of loading on the blade is therefore a combination of coupling due to the Coriolis effect and aerodynamic damping. In forward flight this will also be the case, but will be harder to predict as the loading on blade varies with azimuth's angle.

2.2.2 Flexible blade behavior

Aeroelasticity

Due to flexibility of the rotor blades, the local angle of attack is being affected which causes changes in the lift distribution. These changes will result back into flexing of the rotor blades causing aeroelasticity. This phenomenon starts a loop of effects that may be stable or unstable.

Stress stiffening and coning

The rotor blades are highly flexible but stiffen up when the rotation causes them to be pulled out straight by their masses. This phenomenon is called centrifugal stiffening. The faster the rotation is, the greater the centrifugal force. The helicopter weight can be easily supported by the resulting rigidity of the blades

due to this force. This is a counter reaction to the centripetal force that accelerates the masses towards the rotating shaft to follow a circular path. Both balance each other out.
Adding to the fact that lift is also acting on the blade, the result of these three forces lets the blades assume a conical path. This is observable as the cone shape of the rotor disk of the helicopter in hovering.

Blade modes

Flexibility of the blade is important as the aerodynamic loading depends on the blade shape. As a consequence of the before mentioned aeroelasticity and stress stiffening, the flexibility of the blade shows particular blade responses. The centrifugal stiffening keeps the blades in a state of tension that can be seen as a function of the rotor radius. This gives the rotor blade in operation a particular stiffness distribution that is also dependent on the rotational speed Ω. Normally, the extreme values of the amplitude responses for the modes will shift with rotational speed.
A distinction should be made between flapwise modes, lagwise modes and torsional modes. These modes then contain information on the structural integrity of the blade as the rotation effects the modeshapes and eigenfrequencies. The flapwise eigenmodes experience more stiffening effects than the lagwise modes. These modes are build up as a consequence of structural and rotational stiffness.

De Jong [4] numerically determined the natural frequencies of the first 8 modes of an articulated helicopter rotating blade in terms of the rotor frequency (table 2.1). To be consistent with his research, these ratios will also be preferred for representing the structural stiffness in the blade of the demonstrator.

	Mode #	Ω
1	Lag 1 (rigid)	0.3
2	Flap 1 (rigid)	1.04
3	Flap 2 (elastic)	2.68
4	Lag 2 (elastic)	4.56
5	Flap 3 (elastic)	5.35
6	Torsion 1	5.82
7	Flap 4 (elastic)	9.65
8	Lag 3 (elastic)	11.9

Table 2.1: Helicopter natural frequencies in terms of rotor frequency Ω.

2.3 Effect of cyclic loading

The function 'Generate vertical thrust' was subdivided into three sub-functions i.e. generate rotor torque, control magnitude of the rotor thrust and convert torque in vertical thrust [11]. As forward flight is observed as the extension of hovering, an additional sub-function can be distinguished such as convert torque in forward thrust. To this end the helicopter then uses cyclic pitch which means that the blade pitch is varied sinusoidally. As mentioned earlier, the position of the blade on the rotor disk can be defined in terms of an azimuth angle Ψ. According to Bramwell [1] the blade pitch θ can then be expressed as:

$$\theta = \theta_0 + A_1 cos\Psi + B_1 sin\Psi \tag{2.11}$$

Where θ_0 is the initial collective pitch angle, required to maintain hovering lift. The coefficients A_1 and B_1 correspond to sideways and forward tilting of the rotor axis. As a consequence of this blade pitching, the blade flapping will also be a function of equation (2.11). The cyclic pitch thus allows a periodic component in the relative airspeed experienced by the blade.

2.3.1 Dissymmetry of lift

One other purpose of cyclic pitching is to make the average lift moment on both sides of the rotor disc the same. However, it cannot keep the lift of an individual blade constant at all angles of rotation. In figure 2.6 a blade element in forward flight is shown where uniform inflow across the disc is assumed and coning is neglected. The figure shows the relative airspeed experienced by a blade element. The rotational speed of the rotor allows for a constant component in the diagram. For $0 < \Psi < 180°$ the blade is considered advancing and for $180° < \Psi < 360°$ the blade is retreating. The forward speed can be seen as the sinusoidal component adding speed to the advancing side and subtracting speed from retreating blade. Notice that the speed of the blade in forward motion is an added speed to the constant component. Figure 2.6b shows the generated lift due to the forward speed. As lift is proportional to square of airspeed, the advancing side experiences more lift than the retreating side. A helicopter with a counterclockwise blade rotation would then roll to the left due to this dissymmetry of lift. For this reason, the blade hinges are designed to allow the blade to flap and feather automatically to equalize lift across the rotor disc. As the blade flaps up in advancing side, the angle of attack reduces, allowing less lift to be generated. In the retreating side, the blade flaps back down and increases the AoA again.

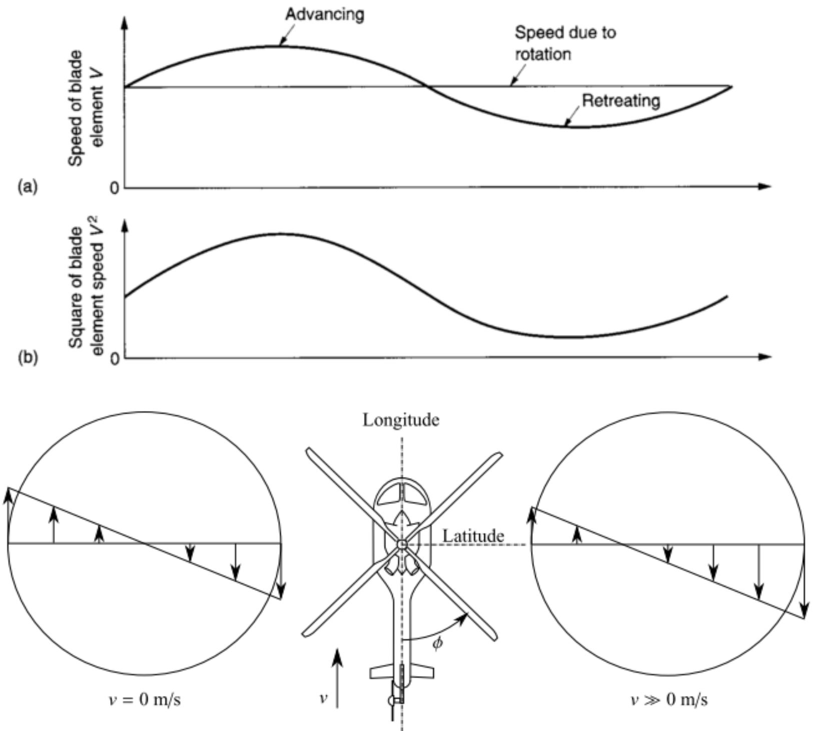

Figure 2.6: Dissymmetry of lift due to cyclic loading with top view representation [4, 24].

2.3.2 Harmonic effects on flapping

Blade flapping happens thus periodically as the blade flaps up and down in the rotation cycle of the rotor. When the helicopter moves forward, there will be an inflow ratio and a collective pitch angle for maintaining lift to stay in the air. The inflow ratio causes a forced blade motion, where the advancing and retreating sides are periodically affected. The forced flapping blade motion can then be expressed as an infinite Fourier series at 1/rev:

$$\beta(\Psi) = \beta_0 + \beta_{1a} cos\Psi + \beta_{1b} sin\Psi + \beta_{2a} cos\Psi + \beta_{2b} sin\Psi + ... \tag{2.12}$$

The lift function thus contains harmonics that are at integer multiples of the rotor speed. As the lift troughs on the two sides of the rotor have different shapes, levels of odd harmonics will exist. The result is that the blades will describe a motion as shown in figure 2.7.

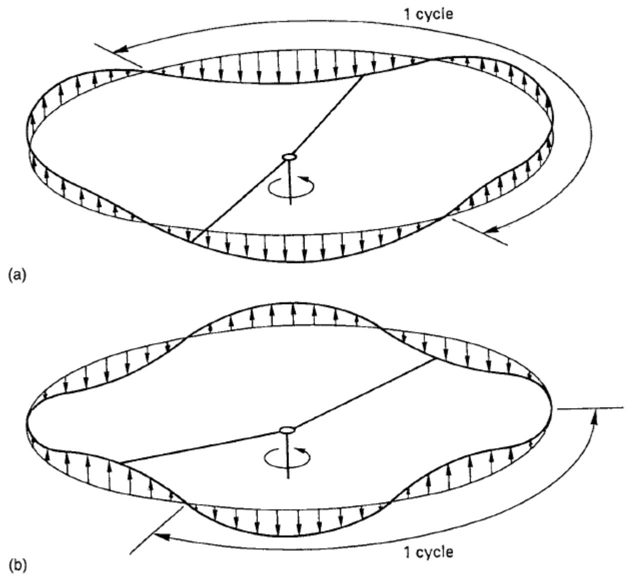

Figure 2.7: 2nd and 3th harmonic flapping.

In forward flight an analytical closed-form solution of the complete flapping equation is difficult to obtain. More pragmatical solutions are to solve numerically or analyze a steady-state response in a periodic form. Hence, also possibilities for conducting experimental investigations.

2.4 Review

This chapter introduces the functionality of forward flight as context of the operation for the rotating blade. The differences between hovering and forward flight are presented with the aim of understanding the numerical work presented by Oosterik and discussing the implications for a more complex operational environment. Special attention is given to the coupling phenomena of Coriolis and aerodynamic forces, because of the interaction between degrees of freedom and how these are more complex in cyclic loading conditions.

Furthermore the chapter focused on the following phenomena:

- The influence of the flapping behavior to the lagging moment, as described by eqn 2.10 for the hovering flight.
- The dissymetry of lift that causes a non-constant, cycling changing loading condition in the forward flight.
- The harmonic response of flexible blades during forward flight.

These scenarios will be used as input for the redesign of the demonstrator in the following chapters.

Chapter 3

Re-design of the demonstrator

From the previous chapter was concluded that the most interesting phenomena to explore by means of a demonstrator are the influence of the lagging moment in the flapping behavior for hovering flight, the dissymmetry of lift and finally the harmonic response of flexible blades during forward flight.
The demonstrator currently available in the Applied Mechanics lab, consists of a hanging, non-rotating blade that allows flapping, lagging and pitching motions (figure 3.1). As the behavior of the rotor blade system in a helicopter's forward flight has been formulated, this can be translated into requirements and measurement strategies for experiments on the RBS demonstrator to represent the effects of a rotating blade. However, as these motions are not coupled to each other, these will need to be introduced. In this section the behavior of the demonstrator will first be re-evaluated and then customized accordingly.

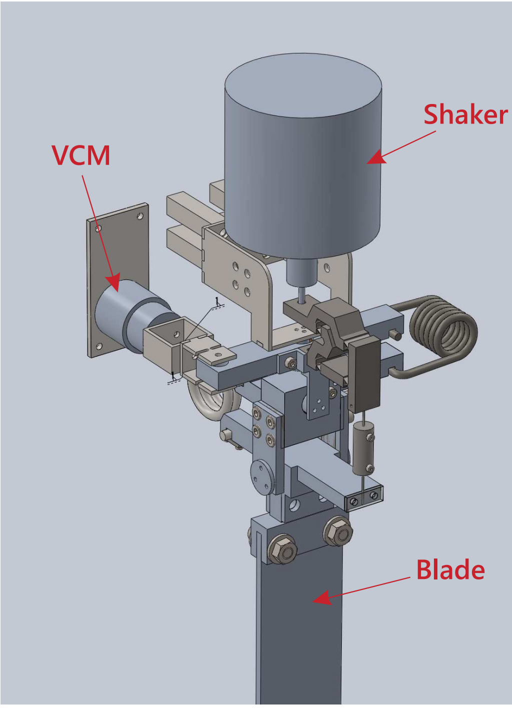

Figure 3.1: The initial RBS demonstrator (without frame).

The various flight conditions in this thesis will be modeled according to an example helicopter rotor blade system with the properties as specified in table 3.1.

Parameter	**Symbol**	**Value [unit]**
Number of blades	N_b	4
Rotor radius	R	8.15 m
Rotor speed	Ω	10 Hz
Chord length	c	0.65 m
Blade thickness	t	0.145 m
Blade mass	m	186.6 kg
Moment of inertia	J_{blade}	2812 kgm^2

Table 3.1: Helicopter blade properties

3.1 Representing the complexity of a RBS with a non-rotating blade

For the demonstrator in this project, the blade will be represented by a non-rotating scaled version of the actual rotor blade. The real helicopter blade is highly flexible and it was clear from chapter 2 that the flexible modes form an integral part of the blade response. Because of the simplification to a simple beam structure, the natural frequencies will ofcourse be different. To represent a similar stiffness distribution of the helicopter blade in the non-rotating blade, it will be important to achieve the same ratio between natural frequencies as specified in table 2.1.

The modal participation of the rigid mode in the blade response is usually larger compared to the elastic modes. The focus will be on achieving the same frequency ratio between the rigid and first elastic mode of the helicopter case. Using a torsion spring in the boundary conditions of the blade allows control of the stiffness distribution throughout the blade when vibrating. As the torsion spring represents a rotational stiffness in the joint, analytical calculations can be performed to achieve the desired ratios.

In section 4.1 will be mentioned that an electrodynamic shaker will be used for the excitation. Because this shaker has an operating range starting at 10 Hz, it is convenient to let the blade have a flapping rigid body frequency above this frequency if it is preferred to excite this mode. In accordance with table 3.1, taking a rotating frequency Ω of 10 Hz for the helicopter case, will lead to the following desired frequencies for the modes in the blade:

$$f_{l_r} = 3Hz \qquad f_{f_r} = 10.4Hz \qquad f_{f_{el}} = 26.8Hz$$

3.1.1 Rigid behavior

The rigid behavior with the addition of a torsion spring on its boundary is comparable to the oscillations of a pendulum. If the hinge is then controlled by a torsion spring, this frequency will increase significantly. The rigid body frequency with a torsion spring is determined starting from the equation of motion:

$$\begin{aligned} &\sum M_0 = I_0\ddot{\theta} \\ \Rightarrow &\frac{1}{2}mgLsin\theta - c\theta = I_0\ddot{\theta} \end{aligned} \tag{3.1}$$

After linearizing around the equilibrium and re-arranging in the "standard form" with $I_0 = \frac{1}{3}mL^2$:

$$\begin{aligned} &I_0\ddot{\theta} + (\frac{1}{2}mgL + c)\theta = 0 \\ \Rightarrow &\ddot{\theta} + (\frac{3g}{2L} + \frac{3c}{mL^2})\theta = 0 \end{aligned} \tag{3.2}$$

The rigid body frequency of this blade with rotational stiffness can then be found with:

$$\omega_0 = \sqrt{\frac{3g}{2L} + \frac{3c}{mL^2}} \tag{3.3}$$

3.1.2 Blade flexibility

The elastic modes in the helicopter blade are the result of the flexibility of the blade. In this research the demonstrator will be used to investigate only flapping and lagging motions and therefore the relevant modes will be flapwise and lagwise bending modes of the blade. These modes can be determined analytically because of the simplification to a simple beam.

For free vibration of an element of a beam, the equation of motion is as follows:

$$\rho A \frac{\partial^2 w(x,t)}{\partial t^2} + EI \frac{\partial^4 w(x,t)}{\partial x^4} = 0 \tag{3.4}$$

The equation contains a second-order derivative with respect to time and fourth-order derivative with respect to x. The free vibration solution is found using the method of separation of variables. From the process a characteristic equation is obtained, of which the solution is assumed to be in the form of:

$$Y(x) = B_1 cos(\beta x) + B_2 sin(\beta x) + B_3 cosh(\beta x) + B_4 sinh(\beta x) \tag{3.5}$$

The terms B_1, B_2, B_3 and B_4 are constants that can be found after the using the boundary conditions where the rotational stiffness c is also accounted for. The complete derivations are given in appendix A. The resulting characteristic equation can then be expressed as a function of the rotational stiffness of the hinge:

$$\begin{aligned} c.cos^2(\beta L) + c.cosh^2(\beta L) + c.sin^2(\beta L) - c.sinh^2(\beta L) + 2c.cos(\beta L)cosh(\beta L) \\ -2EI\beta cos(\beta L)sinh(\beta L) + 2EI\beta sin(\beta L)cosh(\beta L) = 0 \end{aligned} \tag{3.6}$$

The values of β can then be determined numerically, by plotting the equation and finding the intersections with the x-axis ($y = 0$) in Matlab. A rotational stiffness will need to be specified first. For each intersection β found, an eigenfrequency can be computed with:

$$\omega_n = (\beta L)^2 \sqrt{\frac{EI}{mL^3}} \tag{3.7}$$

Having obtained a method for determining the rigid and elastic flapping modes of the blade with a rotational stiffness, the effect on the modes when varying this stiffness is illustrated in figure 3.2. Because the focus lies on the ratio between the rigid and first elastic modes, only these two are shown in the graph. The blade used for this calculation is made from aluminum and has a length of 500 mm. For very low stiffness (hinged) and very high stiffness (clamped) the first natural frequencies remain at 13 Hz and 57 Hz respectively. Notice how the rigid mode line disappears just before coinciding with the elastic mode. This is obvious as the beam approaches a clamped situation, there will no longer be a rigid mode as the joint of the blade is then fixed and the rest of the blade is prone to bending.

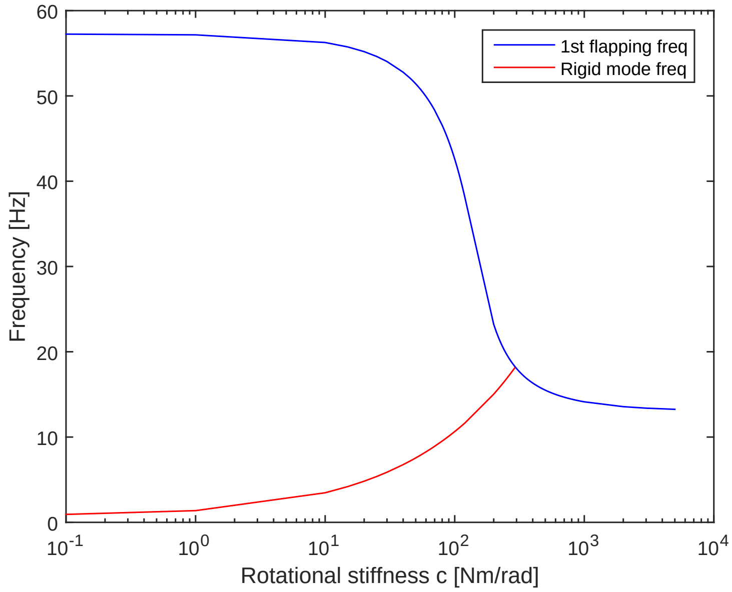

Figure 3.2: Rigid mode and first flapping frequency for varying rotational stiffness in the joint.

Flapwise modeshapes

After determining the mode frequencies of the blade, the analytical mode shapes can be plotted to verify if these indeed correspond to the intended frequencies. Given for example a rotational stiffness $c = 126$ Nm/rad, then for the β values are found:

$$\beta_1 = 6.28 \qquad \beta_2 = 13.47 \qquad \beta_3 = 20.01$$

From appendix A could be seen that three constants are dependent on B_3. Therefore the scaled modeshapes can be graphically presented by assuming $B_3 = 1$, which then give $B_1 = -1$, $B_2 = -0.6433$, $B_4 = -0.9152$ for β_1. The modeshape for β_1 represents the first elastic mode. Figure 3.3 shows this modeshape for varying rotational stiffness. As the rotational stiffness is increasing and blade approaches a clamped configuration in its end, it experiences less bending deformations.

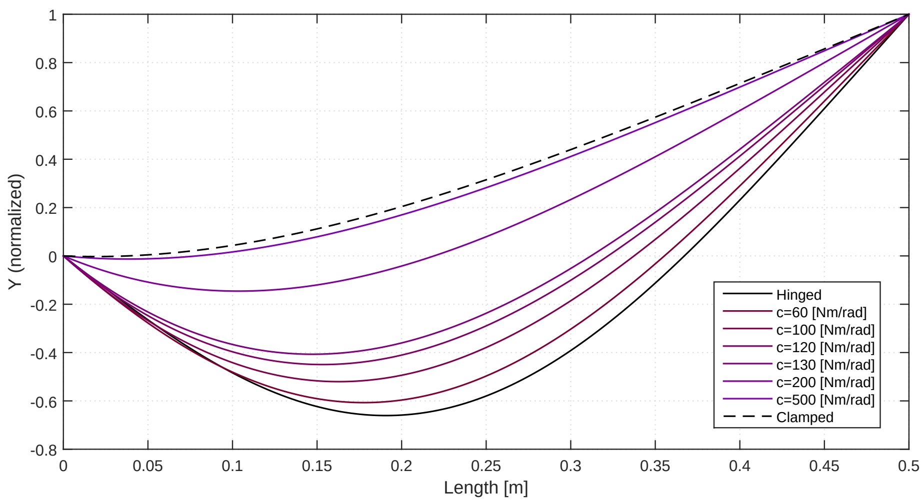

Figure 3.3: The first modeshape for changing rotational stiffness from hinged to clamped.

3.1.3 Evaluating blade dimensions and boundaries

The first elastic frequency is approximately 2.6 times the rigid mode frequency according to table 3.1. The ratio between these modes will be maintained in the demonstrator to resemble the real blade as much as possible. As these modes can be controlled by the method discussed in the previous section, the appropriate dimensions of the blade can be assessed and the selection for suitable torsion springs can be made. To obtain an idea of the effects the blade dimensions has on the modes, table 3.2 shows some iterations for varying thickness, width, length and torsional stiffness. Each section shows the adjusted property in bold.

Dimensions #	Rigid body [Hz]	1st Elast. Flap [Hz]
T4, W50, L500, **c126**	11.9	36.7
T4, W50, L500, **c140**	12.6	33.3
T4, W50, L500, **c100**	10.6	42.6
T4, W50, **L600**, c126	9.1	21.4
T4, W50, **L600**, c140	9.6	19.1
T4, W50, **L600**, c100	8.1	26.4
T4, W50, **L450**, c126	14.0	48.9
T4, W50, **L450**, c140	14.7	45.2
T4, W50, **L450**, c100	12.5	55.1
T4, **W20**, L1500, c126	-	17.7
T4, **W20**, L500, c140	-	17.0
T4, **W20**, L500, c100	-	19.8
T2.5, W50, L500, c126	-	9.6
T2.5, W50, L500, c140	-	9.4
T2.5, W50, L500, c100	-	10.1

Table 3.2: Rigid and elastic modes when varying blade parameters at three different rotational stiffness.

It can be seen from the results that when the rotational stiffness is increased, the rigid mode frequency also increases and the elastic frequency decreases. The latter was also concluded from figure 3.2. Increasing the length of the blade lowers both the rigid mode and the elastic frequency. Decreasing either the width or thickness, the rigid mode frequency disappears and the elastic frequency drops. This is obvious as the blade will then seem to approach a clamped configuration because the inertia in the flapping mode becomes much lower than in the other directions.

The best frequency ratio is achieved with the initial blade and having a rotational stiffness of 140 [Nm/rad]. Using a blade with length of 600mm and c126 also provides a good enough ratio. However due to the height limitations of the demonstrator a longer blade is not an option. After obtaining the required rotational stiffness, the necessary torsion springs for flapping and lagging can be selected.

3.2 Evaluation of the flap-pitch mechanism

This mechanism enables flapping excitations while the blade is performing pitch movements by a voice coil motor. The mechanism centers the flapping actuation point around the pitch axis. Previous research concluded that the pitch-flap flexure was too stiff and resulted in incorrect force transmissions onto the blade. According to the previous section the rigid flapping mode is set at 11.9 Hz, which means that this flexure mechanism should have a good transmission ratio around this frequency.

ANSYS Mechanical (Workbench) can perform modal and harmonic analysis on a structure. The modal analysis determines the free vibrations of the mechanism and revealed that the first mode, which corresponds to the bending mode in flapping direction, is found at 140 Hz (figure 3.4). As the operating range of the demonstrator is preferred to be between 0 and 50 Hz, this mode is too high which might result in high stiffness in the specified range. The consequence of this is that the flapping deflections will then be too small.

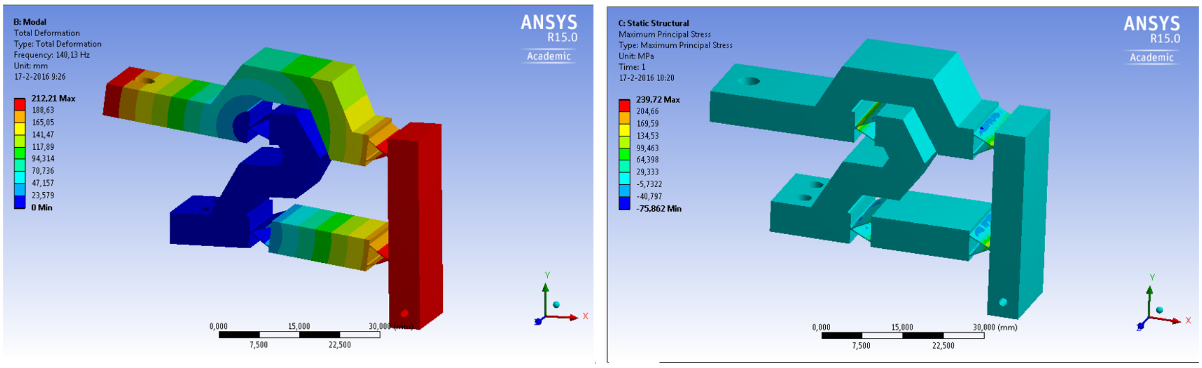

Figure 3.4: Modal and static analysis of the initial flexure.

A harmonic analysis determines the steady-state sinusoidal response to sinusoidal varying loads all acting at a specified frequency. This is useful for determining the transmission ratio of the flexure mechanism. The analysis shows that the displacement in the flexures end in the frequency range of interest is only 0.33 mm (figure 3.5). These are relatively small displacements and correspond to angles of approximately 0.25°. As expected from the modal analysis, the largest deflection is found at 140 Hz.

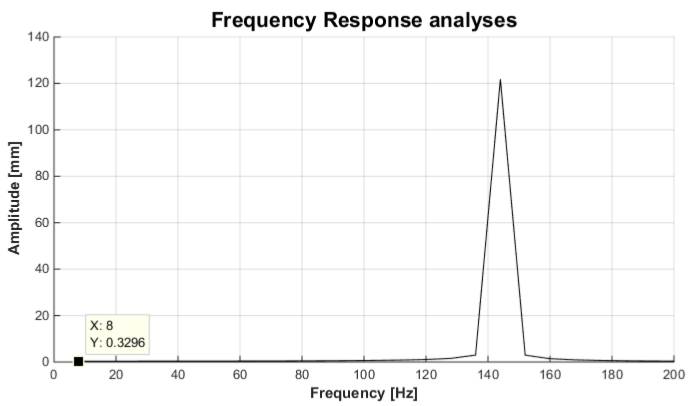

Figure 3.5: Harmonic analysis of the initial flexure.

The final investigation concerns a static analysis, which shows that there are no stresses above the yield stress and are all well under a third of the yield stress, meaning no fatigue issues.
Based on the performed analyses, there is possibility for improving the flexure mechanism to obtain a good transmission ratio in the range of 0-50 Hz. In the following section, alternative concepts will be presented.

3.2.1 Alternative concepts

Three concepts are presented, where the starting point involves a concept that is based on minimal changes in the initial mechanism.

Concept 1: Minimal changes

This design inspects if the initial flexure concept can be used with minimal changes i.e. reducing the width of the hinges to lower stiffness and adding mass to the moving beam. Both changes imply a lower bending frequency, as ω is proportional to $\sqrt{k/m}$.

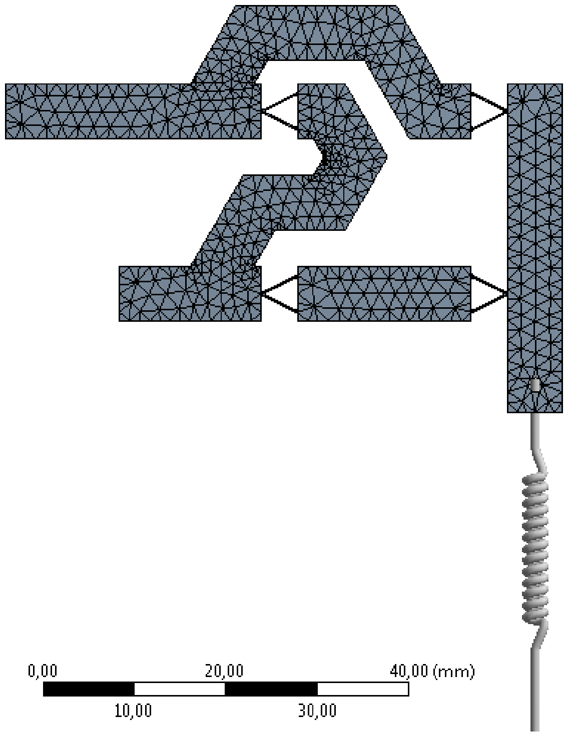

Figure 3.6: Simulating a rotational stiffness with a linear spring.

The concepts are also analyzed with the effect of the torsion spring. This has been implemented in Ansys Workbench by simulating the flap torsion spring as a linear spring with stiffness K (figure 3.6). For incremental rotations θ, the torques as a result of rotational and linear stiffness can be calculated with:

$$T = c\theta \qquad \text{and} \qquad T = FR = (K\theta R)R \tag{3.8}$$

For equal torque, the equations can be combined and the required linear stiffness can be found with:

$$\begin{aligned} c\theta &= K\theta R^2 \\ \Longrightarrow K &= \frac{c}{R^2} \end{aligned} \tag{3.9}$$

For $c = 126Nm/rad$ and $R = 50mm$, the linear stiffness of the spring $K = 2.5N/mm$. Simulations have been carried out in Ansys Workbench and the results are summarized in table 3.3. The frequency responses of the flexure mechanism can be seen in figure 3.7. For the final experiments with this mechanism it is important to maintain a linear response over the operating range to avoid sudden increases in responses when hitting the bending frequency. Therefore the table also shows the range up till the response amplitude is within 20% of the initial response, which can be considered a linear range.

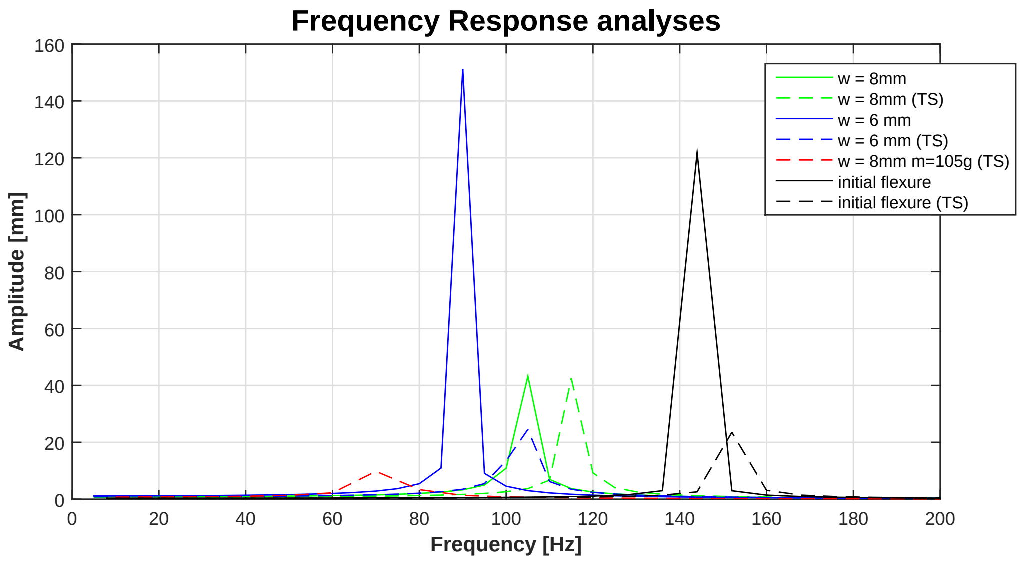

Figure 3.7: Frequency response analyses of the flexure with minimal changes.

	Bending mode [Hz]	Peak stress [MPa]	Linear response
w = 8mm	104	467	$<$ 40 Hz
w = 8mm (TS)	116	376	$<$ 40 Hz
w = 6mm	88	463	$<$ 30 Hz
w = 6mm (TS)	96	345	$<$ 40 Hz
w = 8mm, m = 105.11g (TS)	73	292	$<$ 25 Hz

Table 3.3: Flexures with minimal changes.

The effect of a rotational stiffness is also noticeable in this mechanism and proves to be of significance for the transmission ratio. The transmission ratio of the mechanism decreases with the added rotational stiffness of the torsion spring, while the bending mode increases. Analyzing the complete pitch-flap mechanism including the torsion spring, it can be concluded that these act in series as the total deflection of the flapping arm equals the sum of deflections of the torsion spring and flexure mechanism. Therefore is valid:

$$\frac{1}{c_{total}} = \frac{1}{c_{TS}} + \frac{1}{c_{flexure}} \tag{3.10}$$

This alters the intended boundary conditions of the RBS demonstrator and therefore the ratio between rigid mode and elastic flapping frequency will also change.

Concept 2: Cross-flexure hinges

This concept incorporates the cross-flexure principle (figure 3.8). These types of flexures allow larger angular rotations about an axis and therefore less stiffness. The bending mode is reduced significantly to 39 Hz and has linear response up to 25 Hz. The displacement of the mechanism is 1.58 mm and corresponds to angles of 1.8°.

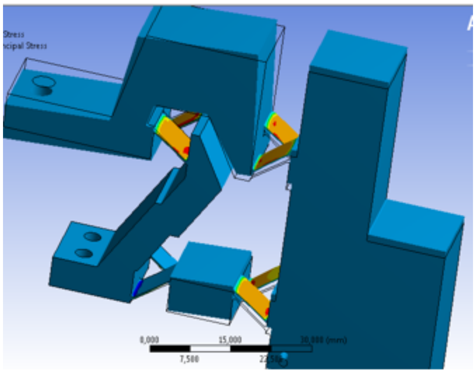

Figure 3.8: Flexure with cross-flexure principles.

Concept 3: Lever mechanism

Introducing a fresh alternative which differs completely from previous concepts allows for a more simple design. Based on a simple hinge principle, a transmission ratio of 1:1 can be obtained. The mechanism is designed to fit into the same dimensions of the flexure mechanism, where the flap hinge will still be connected by 2 sprits and a tube. Now only the rotational stiffness of the torsion spring determines the total stiffness in the boundary condition of the rotor blade. For the pivot point a bearing can be used (GLI BBF 101320).

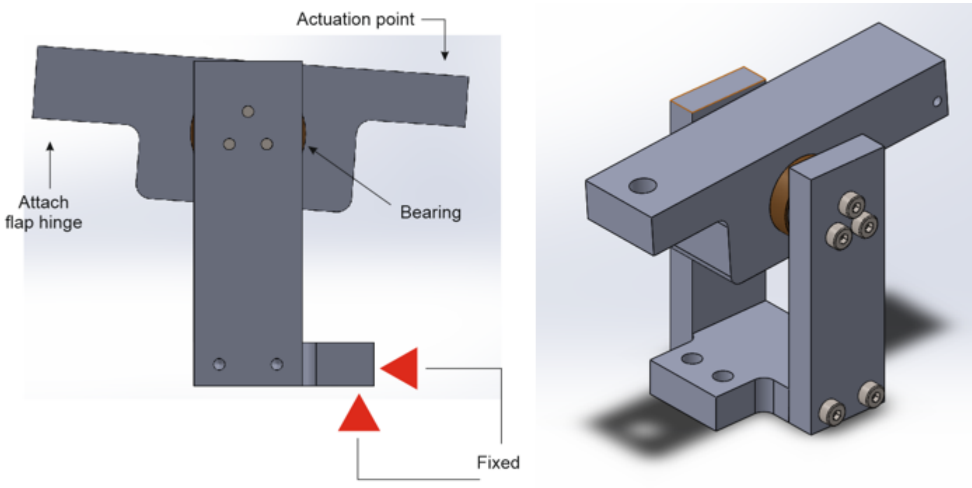

Figure 3.9: Lever mechanism.

Final concept

The problem of the pitch-flap mechanism is solved, by introducing concepts where the response amplitudes are increased due to stiffness alterations. Although the responses of the first two concepts are improved, they still depend on the rotational stiffness of the torsion spring used. The last concept is independent of the torsion spring and offers a direct transmission of forces from the shaker to the blade.
Furthermore concepts 1 and 2 have to be manufactured by Electrical Discharge Machining (EDM). As concept 2 also consists of cross-flexures, these will have to be assembled in the part, because EDM only works with a single piece of material. Concept 3 introduces less manufacturing complexity as the parts can be made individually and assembled with screws. Concerning manufacturing costs, concepts 1 and 2 are made from Titanium, while concept 3 is made from Aluminum. The first two are thus more expensive. In conclusion, concept 3 is chosen as this offers the best solution for the intended test to be performed.

3.3 The lagging mechanism

The lagging motion of the demonstrator showed some play in the hinges. When performing analyses in the frequency domain these can affect the measurements. After careful inspection of the motion, it could be seen that the play occurs due to the non-fixed position of the 'lagging section-block' to its top section. The block is moving axially along the lag-axis. As a solution the block is attached to another bearing with back end at the other side to prevent movement.

Concerning the excitations, the lagging motion can be actuated through a mechanical coupling, where the lagging is directly coupled to the flapping. A strategy more convenient for allowing a variety of coupling cases, is one controlled by a program. Both of these methods will be discussed next.

Mechanical coupling

In this configuration, the lagging motion is directly coupled to the flapping motion by extending the flap-pitch mechanism with a lagging arm and attaching this to the flapping lever with sprits. The idea is depicted in figure 3.10). When exciting flapping, both motions will then be excited.

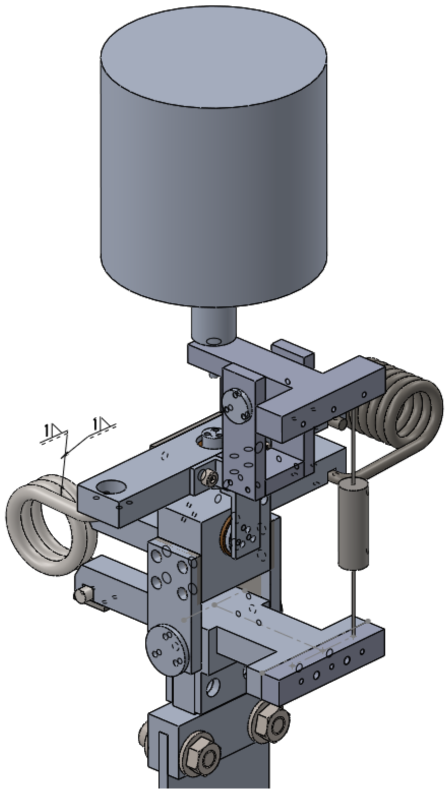

Figure 3.10: Integrated lag lever in the flap-pitch mechanism introduces the mechanical coupling.

The controlled coupling

This configuration is possible due to a second actuator (shaker). By directly extending with a lag lever, the lagging can be performed in a controlled way (figure 3.11). The shaker will then have to exert a force on the lever that is coupled with the flapping excitation through a software setup in LabVIEW.
For the lagging arm a length of 20 cm is chosen to allow enough distance from the frame to attach the shaker. As the amount of exerted force can be controlled through the program, the arm length can be fixed.

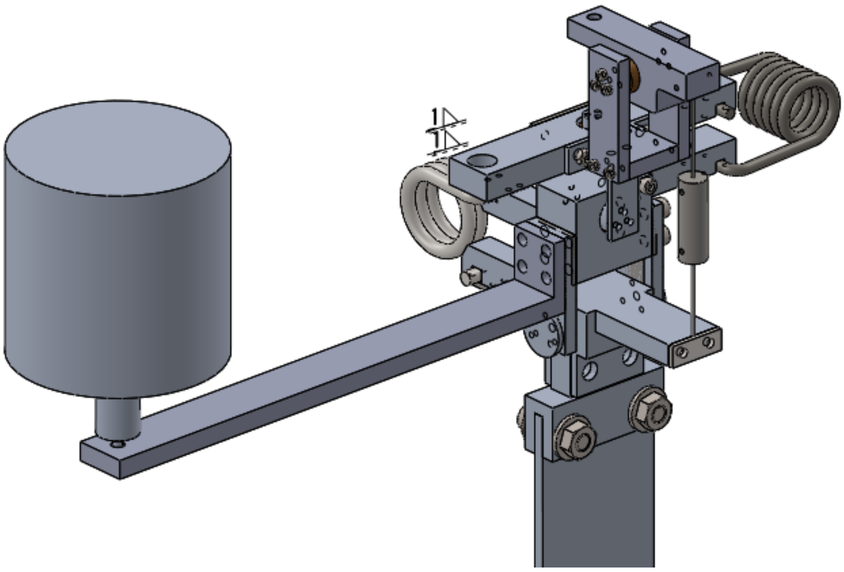

Figure 3.11: The extended lag lever in the demonstrator controlled by a second shaker.

Final concept

The final concept for lagging will contain both configurations. As both can be independently integrated into the demonstrator this will allow the possibility to have a setup where all three DOFs could be excited with a fixed coupling and a setup where only the flapping and lagging can be excited but in a variety of coupling configurations.

3.4 Actuation strategy

The actuation on the demonstrator will be done according to the previous discussed loading on the blade of a helicopter in forward flight. The coriolis coupling and harmonic distortion are the most important cases to investigate.

Harmonic distorted inputs

The harmonic motion can be obtained by using a sinusoidal signal as excitation signal. To simulate the distortion in the inputs signal as explained in section 2.3.2, this sinusoidal signal should contain higher harmonics. By introducing the uneven harmonics of the base excitation in the total signal output, the resulting motion can be achieved as perceived in figure 2.7. To simplify the investigations, only the motion with uneven harmonics will be considered.
Consider a sinusoidal signal of 13 Hz, figure 3.12 shows the resulting truncated signal as a summation of its next 2 uneven harmonic signals c.q. 39 Hz, 65 Hz. This strategy will be implemented in the custom excitation program as explained in section 4.1. The truncation will be related to the flapping speed.

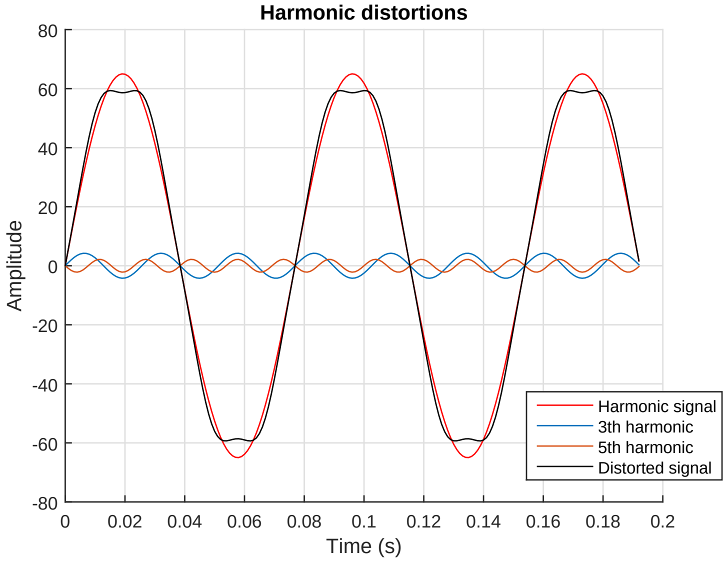

Figure 3.12: The harmonic distorted excitation signal.

Implementing the Coriolis coupling

It could be seen from section 2.2.1 that the Coriolis moment occurs in lagging direction when the blade is flapping. Because the blade in the demonstrator is not rotating, this "resulting" moment will have to be enforced. The ratio of this Coriolis moment with respect to the flapping moment, can be derived from equations 2.9 and 2.10. Assuming $I_{zz} \approx I_{xx} + I_{yy}$, then the ratio of moments simplifies to:

$$\frac{M_z}{M_y} = \frac{-2\Omega\dot{\beta}sin\beta}{\dot{\beta} - \Omega^2 sin\beta cos\beta - (\Omega^2 sin\beta m e_F x_g R^2/I_{yy})} \tag{3.11}$$

The values from table 3.1 are used for the case study. The flapping angle is set to 0.1 radians. The helicopter blade is designed to flap closely to the rotor speed. As the rigid flapping mode is found at 1.04 times the rotor speed, the flapping speed angle will be assumed constant and set at 65.34 rad/s. This then gives a ratio for the moments of $M_z/M_y = 1.89$. To obtain the effects of the coriolis coupling, the force inputs of the demonstrator should then be applied according to this ratio.

3.5 Final Assembly

The demonstrator has been re-designed to allow cyclic loading as perceived in a helicopter in forward flight. The additional consequence that involves the Coriolis coupling can also be simulated in the setup when the flapping and lagging are actuated simultaneously. The complete setup is shown in figure 3.13.

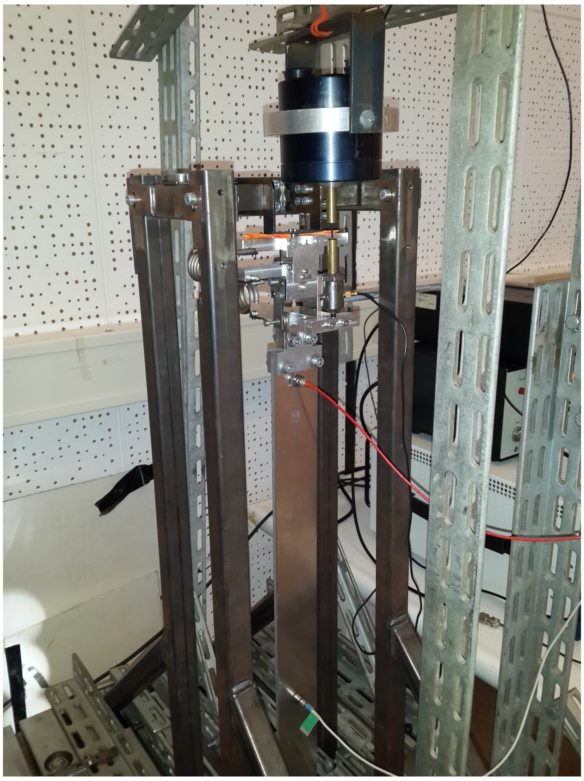

Figure 3.13: The final assembly of the demonstrator setup.

Chapter 4

Experimental setup and verifications

In this part the experimental setup will be presented. Verification tests will be done to determine if the force transfer from the shakers on to mechanisms are working properly. This is crucial to achieve the desired coriolis coupling. Torsion springs with three different rotational stiffness will be used that allows the blade to have different modes. This will also be verified experimentally with modal analysis. The complete scheme for this is shown in figure 4.1. By assuring the correct inputs on the blade, the resemblances to operational loading will be obtained and the behavior of the blade can be analyzed.

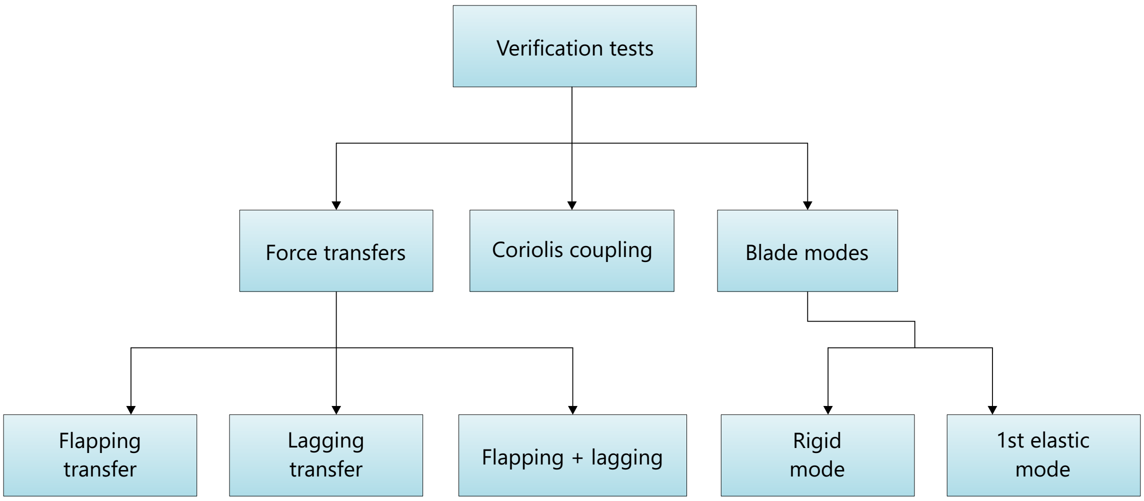

Figure 4.1: Schematic of the verification tests on the demonstrator.

4.1 The setup

The experimental setup to actuate and monitor the blade in the demonstrator consists of 2 shakers and 3 accelerometers (fig 4.2). The additional hardware required to aid these devices are listed in table 4.1. For simultaneous actuations of both shakers, the NI PXI could not be used since it contained only 1 output channel. Therefor the NI9269 module was used, which contained 4 output channels. The input signals were then generated from a separate computer. Since the steady response of the setup was required for analyses, the actual input signals on to the demonstrator will also be measured to find correlations. Force transducers were then placed between the shakers and the demonstrator points of impact. The accelerometers are mounted on specific locations of blade that will measure the response of the blade's base, middle point and tip (figure 4.3).

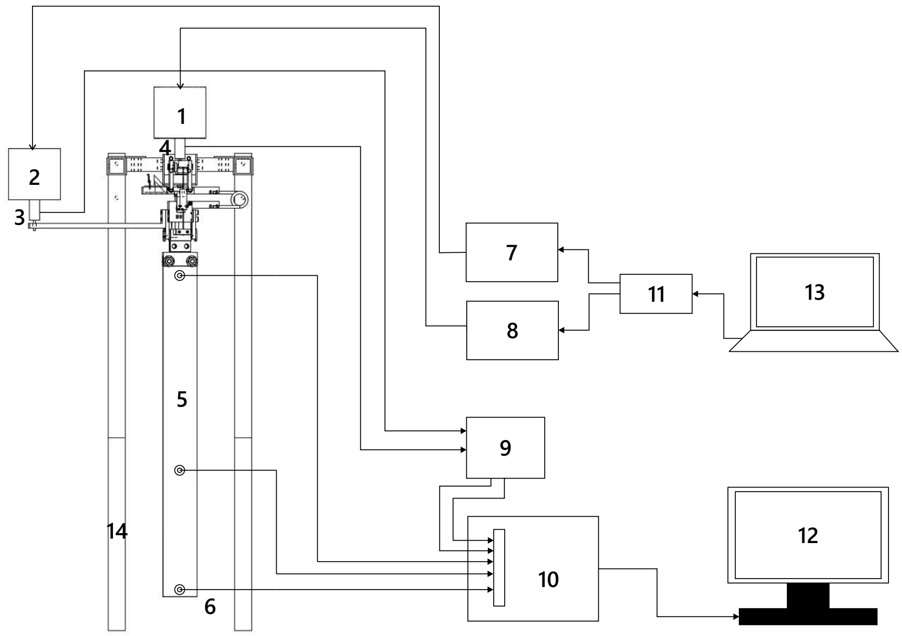

Figure 4.2: Schematic of the experimental setup

#	Description	Hardware	#	Description	Hardware
1	Shaker 1	B&K 4810	8	Power amplifier	TEAC A-H380
2	Shaker 2	B&K 4810	9	Conditioning Amplifier	B&K Nexus
3	Force sensor 1	B&K Type 8001	10	NI DAQ	NI PXI-1042Q
4	Force sensor 2	B&K Type 8001	11	Analog output module	NI 9269
5	Aluminum blade	L = 500mm	12	Sound and Vibration measurement system	PC
6	Accelerometer (3x)	Isotron Endevco 256-100	13	Labview signal generator	Laptop
7	Power amplifier	B&K Type 2706	14	Frame (Demonstrator)	

Table 4.1: Required hardware.

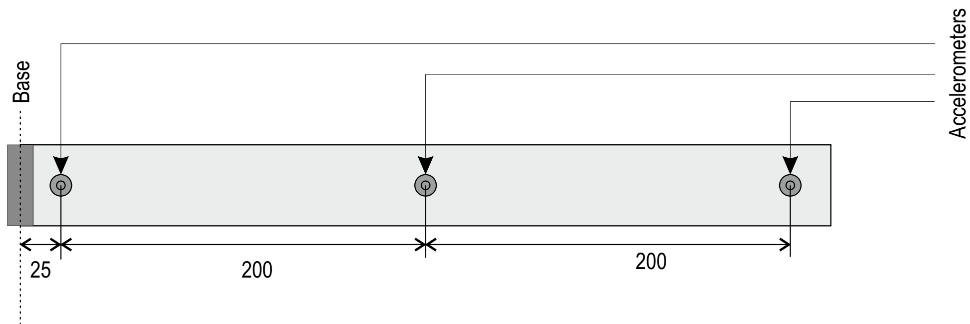

Figure 4.3: The accelerometer locations on the blade.

Software

For the ‘controlled coupling‘, simultaneous actuation signals needed to be generated from a separate computer. A LabVIEW program was then developed, where both flapping and lagging signals were generated with a sine wave generator and passed to the DAQ Assistant. A while-loop around the program was necessary to keep the channels on the DAQ Assistant open while the signal could be generated continuously. Without this loop, the module would open and close for each sample and unwanted delays will occur in the input even as the problem of generating non-continuous signals for frequency that were not multiple of 10.

In section 3.4 was highlight how harmonic distorted signals can be created with a sum of three sinusoidal signals that are an uneven multiple of the base frequency. The LabVIEW program offers the possibility to add up to the 2nd uneven harmonic to the excitation signal. The scheme is illustrated in figure 4.4. All measurement data will still acquired with the Sound and Vibration Measurement system available on the NI PXI Computer in the Lab.

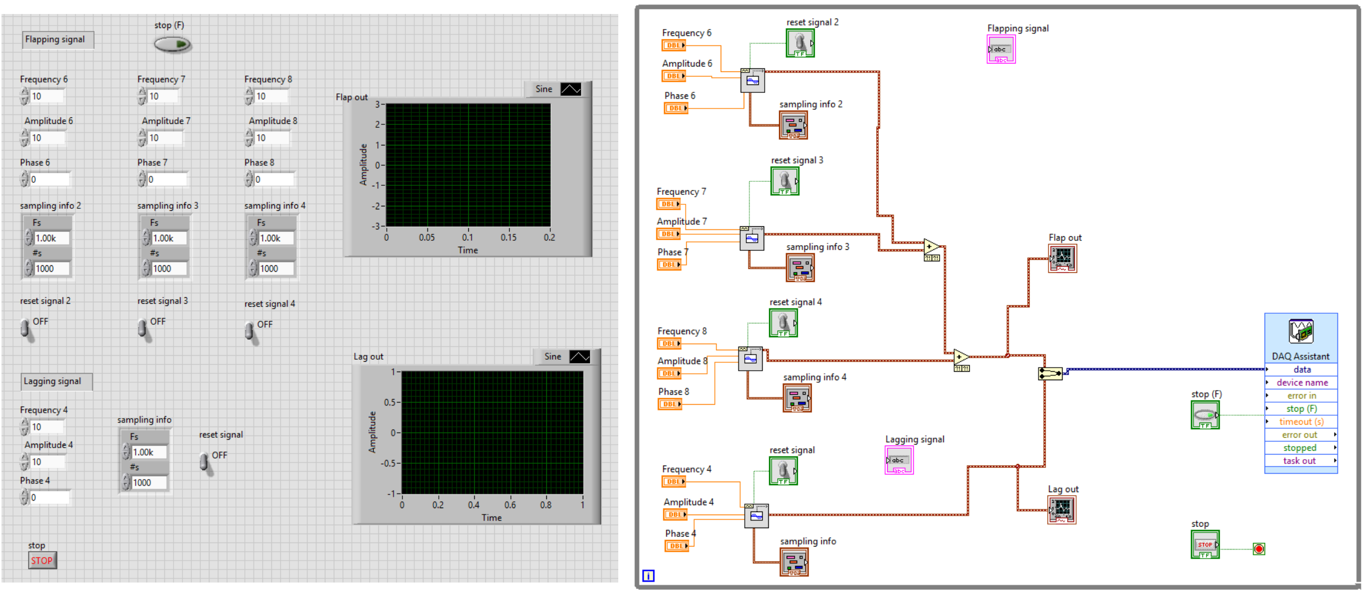

Figure 4.4: Labview control panel.

4.2 Verification operational behavior

After the experimental setup was created, the verifications test of the demonstrator could be performed. To realize the intended effects in the blade, the inputs on to the demonstrator mechanisms must be transfered as expected. The force transfers from the shaker will first be investigated.

4.2.1 Shaker force transfers

Flapping mechanisms

For this investigation a sine excitation with a fixed frequency of 13 Hz was used. The transfer from the shaker onto the flap-pitch mechanism was measured first by placing a force transducer between the shaker and the mechanism. The input signal from the force sensor was heavily distorted and clearly not sinusoidal as intended. The initial explanation to this problem, was the existence of feedback from the demonstrator on to mechanism, which resulted in feedback on the shaker input as well. To solve this problem, more mass of the shaker was required to reduce the feedback effects. Therefore a bigger shaker was mounted. The strategy proved to be correct, as the input signal had a better resemblance to a sine signal. However, due to the added-mass and the higher forces that were working on this mechanism several other problems occurred. The measurements were inconsistent, which revealed that the mechanism was deforming at each test. Figure 4.5 shows that the sprit connection in the mechanism deformed due to the larger input deflections. Furthermore, the base of the mechanism which was attached with two M3 screws to the demonstrator, showed some bending as well. This mechanism could not be used anymore for further testing. The sprit connection should be stiffer to withstand the larger deflections and the base of the mechanism should be fastened more robustly to the demonstrator when using a bigger shaker.

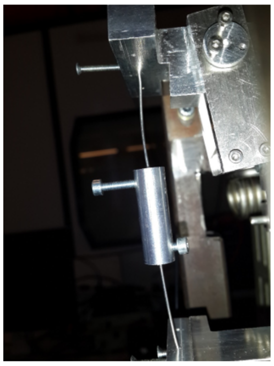

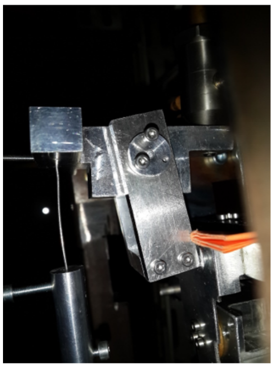

Figure 4.5: The deformed mechanism after testing.

The flap-pitch mechanism was then removed from the demonstrator and for next experiments the shaker was mounted directly on the flapping lever. A fragment of the steady-state transfer force from the shaker on to this lever can be seen in figure 4.6 and will be considered the input force to the system for further experiments. As the signal does look harmonic and definitely periodic, the question remains if the signals is in fact pure sinusoidal as intended.
The fast Fourier transform (FFT) is a mathematical formula that relates a signal sampled in time or space to the same signal sampled in frequency. From the FFT should be clear if the input signal is indeed sinusoidal as the there will be only one peak at 13 Hz in the frequency plot. In figure 4.7 can be seen that the FFT shows additional peaks at 30 and 45 Hz. As these are integer multiples of the base frequency, this means that the system could be sensitive to harmonics of the excitation signal. Compared to the base frequency, the peak of the harmonics are far less and could therefore be disregarded. When running the actual experiments, further investigations need to be done to assess the influences of these harmonics on the results.

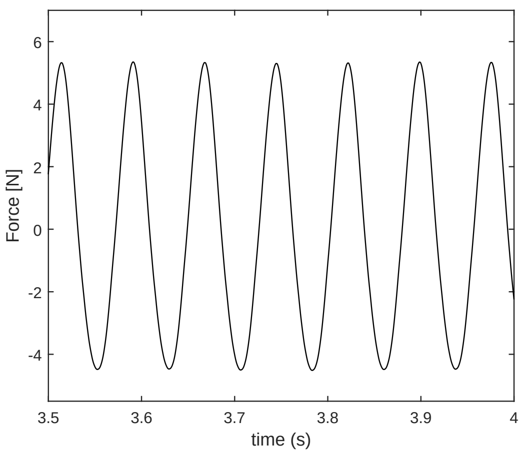

Figure 4.6: Sine input of 13 Hz

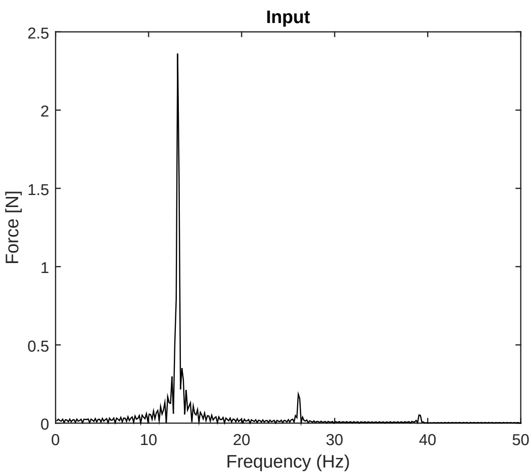

Figure 4.7: The input in the frequency domain.

Lagging mechanism

As the flap-pitch mechanism failed, the coupled lagging that was integrated in this mechanism can not be used anymore. Therefore the second option will be explored; the 'controlled coupling'. The next input to inspect is then from the lagging shaker on to the lagging lever. From the steady-state fragment in figure 4.8 can already be seen that this signal is also not pure sinusoidal and shows distortions in the maximum points. The presence of harmonics can also be verified from the FFT plot.
Because of these occurring harmonics, an attempt will be made to see if an operational setting can be established where these effects are reduced. By determining an appropriate gain where the base excitation amplitude is larger than these harmonics, the influences may be neglected.

Two configurations, at lower and higher than the previous used gain will be used to provide a reasonable assumption of the gain influences. Figure 4.9 shows the input for half the gain used in the previous analysis. This will be considered a low gain. Figure 4.10 shows the input for twice the gain used and will be considered high gain. From these two plots it is clear that the distortions still remain. However, for the low gain the 45 Hz harmonic seems to reduce and almost disappear.

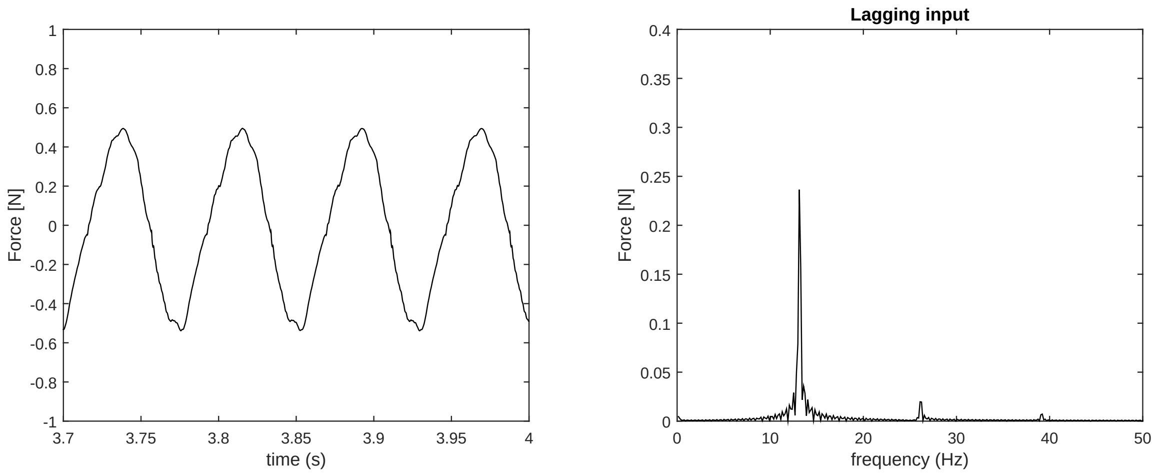

Figure 4.8: Lagging sine input of 13 Hz (a) Time plot (b) Frequency domain.

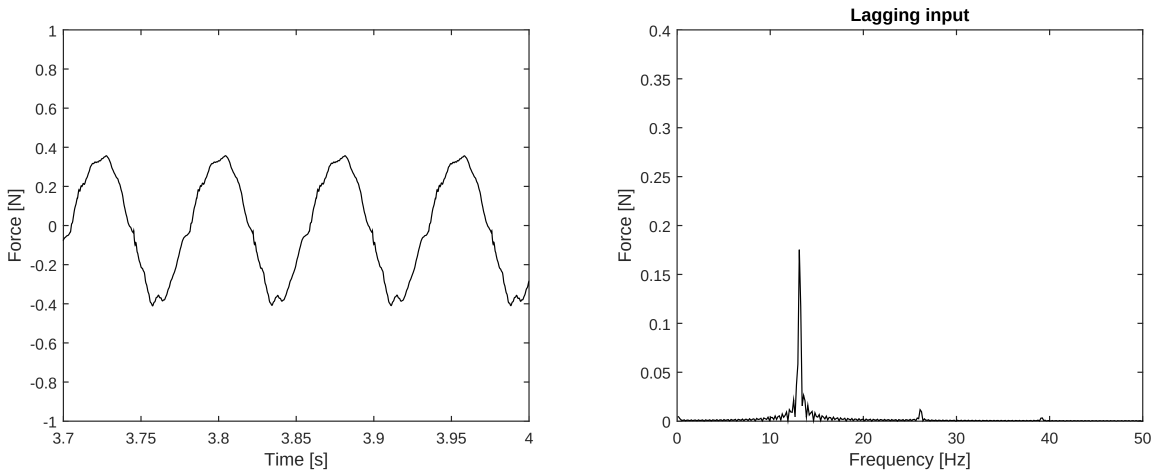

Figure 4.9: Sine input of 13 Hz with 1/2x gain (low) (a) Time plot (b) Frequency domain.

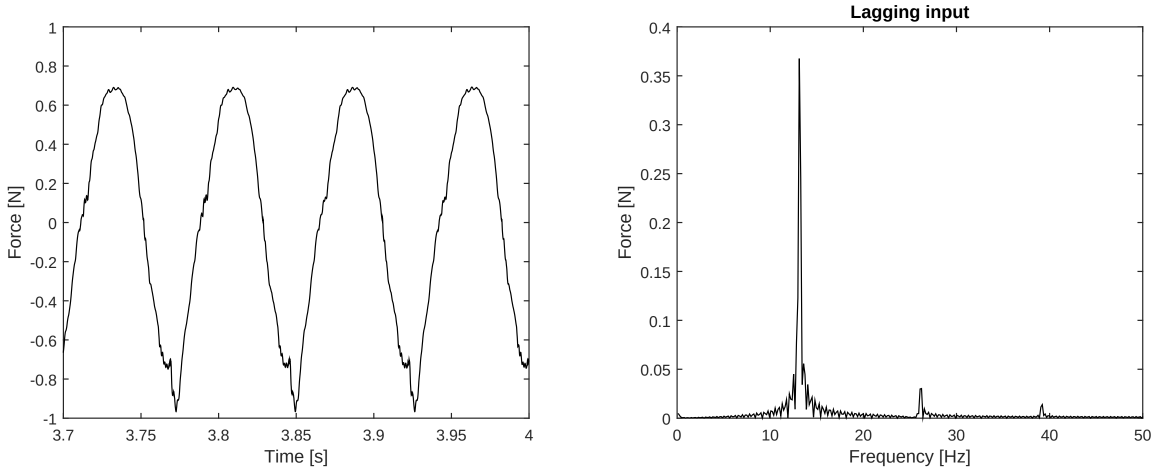

Figure 4.10: Sine input of 13 Hz with 2x gain (high) (a) Time plot (b) Frequency domain.

Another attempt will be made, with a signal of a higher frequency. Figure 4.11 shows the input for a 20 Hz sinusoidal signal with low gain. This signal has more resemblances to the base excitation signal and the harmonics are significantly lower. It should however be noticed that at the same low gain of the shaker, the input force reduces almost twice. It can be concluded that both gain and excitation frequency need to be taken into account when performing the experiments. As harmonics are unavoidable in real life setups due to the clamping of the excited objects, this behavior in the demonstrator proposes limitations to the lagging operational range.

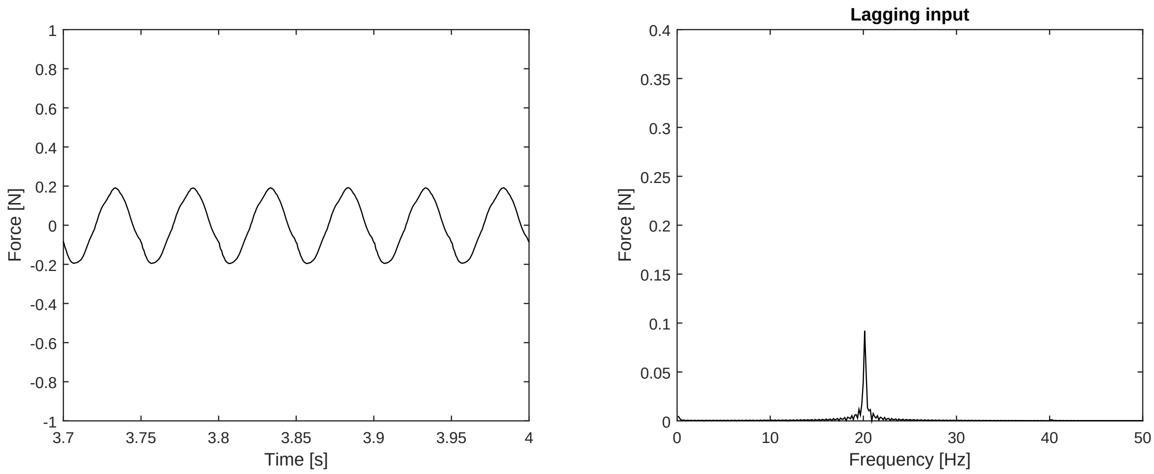

Figure 4.11: (a) Sine input of 20 Hz with low gain (b) The input in the frequency domain.

4.2.2 Simultaneous flapping and lagging

Simultaneous flapping and lagging is the result of the Coriolis coupling. With the limitations of the lagging amplitudes found earlier, the intended Coriolis coupling will have to be adjusted to the setup. First will be inspected if the simultaneous flapping and lagging motions can be excited as expected.

The time waveforms in figure 4.12a shows the flapping input signal when lagging is excited with a low and high gain. It is already clear that the lagging input in the demonstrator influences the flapping input significantly. As the demonstrator is build modular, the flapping hinge is attached to the lagging hinge, causing the flapping shaker to move slightly along with the motions of the lagging mechanism.
Theoretically, the lagging motions should not be influenced by flapping, but as figure 4.12b plots both lagging inputs, it is clear that there is some feedback. In the previous chapter was shown that when the

lagging gain is too high, the input becomes distorted. During the experiments in this chapter, the flapping shaker is also attached to the demonstrator while testing lagging and already results in distortions at lower lagging amplitudes than tested before. It can be concluded that the flapping setup does affect the lagging input. Further testing will have to account for this phenomena and the experiments will have to be adapted to the demonstrator's limitations in its capabilities.

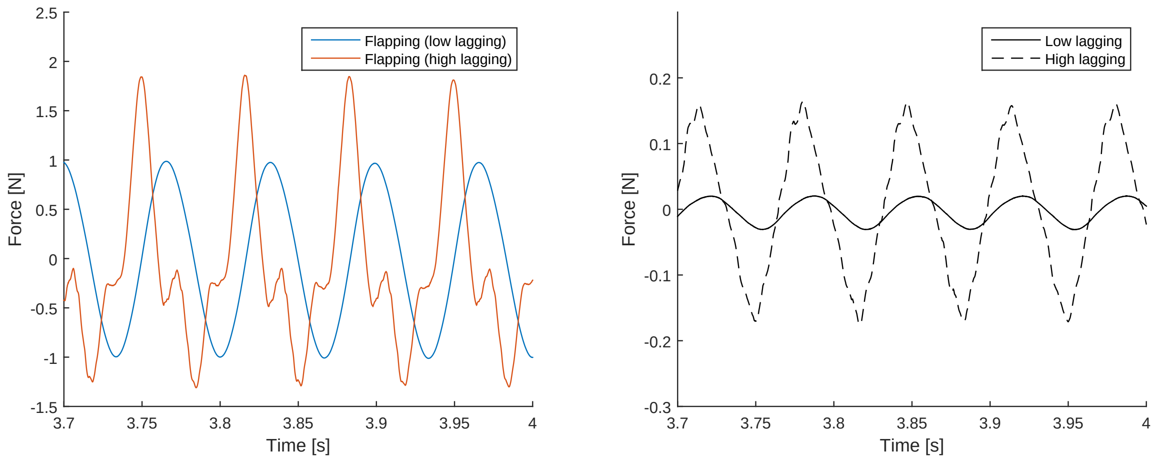

Figure 4.12: Flapping inputs with low and high gain lagging. b) Lagging inputs with low and high gain.

The lagging capabilities in the frequency domain will be investigated next. As concluded earlier, higher gain lagging results in a distorted input signal. The effect of this distorted signal is noticeable in the flapping input, which triggers harmonics of the excitation frequencies in the flapping input (figure 4.13). The lagging input is less affected by the flapping input when its gain is set low. Therefore the experiments in the next chapter will be performed with a low lagging gain of 0.05 N at most from the shaker.

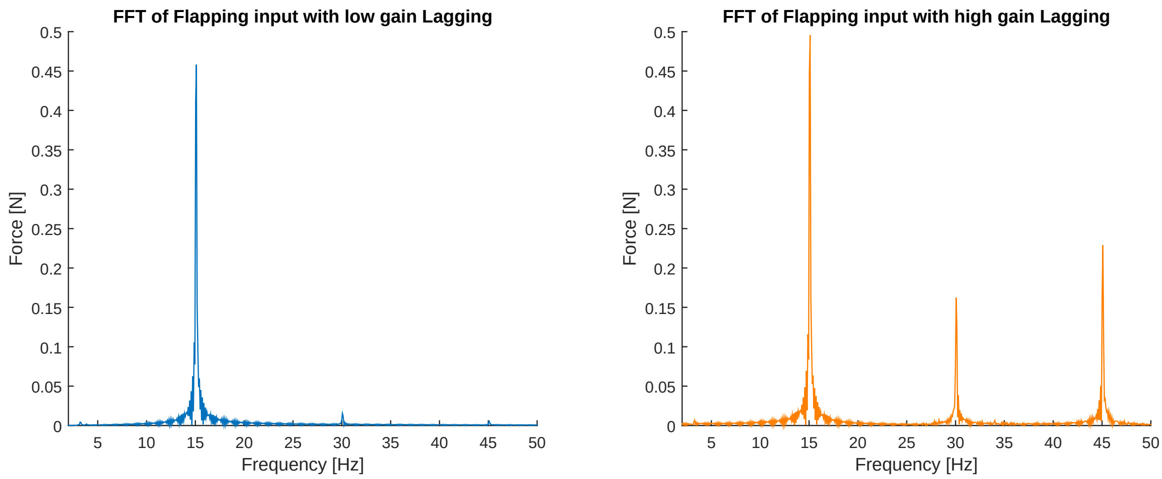

Figure 4.13: Flapping inputs with low and high gain lagging.

The maximum force exerted on the lagging mechanism can be 0.05 N. This corresponds to a lagging moment of $0.05N * 0.2m = 0.01$ Nm. With a flapping force of 1 N, the ratio between lagging and flapping becomes $M_L/M_F = 0.2$. The expected ratio was 1.89 for the Coriolis coupling. Due to the smaller lagging contributions, the effects might not be as large when using the intended ratio. However, there should be a noticeable effect as the motion is now a 2 DOF motion.

4.3 Modal characterization

In this section, the modes of the blade as determined in section 3.1.2 will be verified experimentally. The modes or resonances are determined by the material properties such as mass, stiffness, and damping properties, and boundary conditions of the structure. Therefore the natural frequencies of the blade are a suitable characteristic of the blade configuration with its rotational stiffness.
Because the initial configuration with flap-pitch mechanism can not be used for the experiments, the shaker is directly mounted on the flapping hinge.

4.3.1 The Experimental Modal Analysis

The modal parameters are found using the Experimental Modal Analysis, also known as modal analysis or modal testing. The analysis determines the natural frequencies, damping ratios, and mode shapes through vibration testing. The basic idea of EMA is to excite a structure with a known input force and measure its vibrational response. When the structure is excited, its response exhibits a sharp peak at a resonance when the forcing frequency is equal to its natural frequency.
The data should first be transformed to the frequency domain with the Fast Fourier Transform. Subsequently, Frequency Response Functions (FRF) are estimated that correlate the outputs to the inputs as a function of frequency. The FRF is therefore a measure of how much displacement, velocity, or acceleration response a structure has at an output point, per unit of excitation force at an input point. The modeshapes are then obtained by plotting the magnitudes of the FRFs at the natural frequencies.

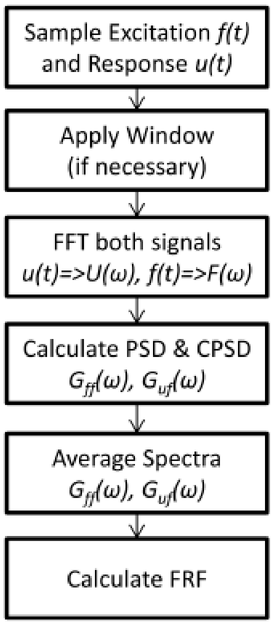

Figure 4.14: Schematic overview of EMA.

4.3.2 Blade modes verifications

The modal parameters are found using the Experimental Modal Analysis. For the excitation a linear sweep signal is used from 0 to 200 Hz in a time frame of 7 seconds. Between the shaker and the demonstrator a force transducer measures the input force. The accelerometers provide the output vibration data of the blade that will be converted into the frequency domain with the help op ME'Scope. Clear peaks that correspond to the modes of the blade are then identified. For the experiments, three torsion springs with different torsional stiffness will be used. Therefor, modal characterization on the setup was done for each of the Torsion springs (TS). The theoretical rotational stiffness could however not be achieved in the torsion springs due to inaccuracies of the spring leg lengths. The actual lengths were then measured and the corresponding modes were again calculated and presented under 'Implemented' in tables 4.2 and 4.3. After performing the EMA, the measured rigid modes and 1^{st} elastic modes for flapping are shown in this table.

Rigid Body	**THEORETICAL**		**IMPLEMENTED**		**MEASURED**	**DIFFERENCE**
	Rot. Stiff. [Nm/rad]	**[Hz]**	**Rot. Stiff. [Nm/rad]**	**[Hz]**	**[Hz]**	**[Hz]**
Torsion spring 1 (hard)	126 (100%)	11.9	112	11.3	8.7	-2.6
Torsion spring 2 (medium)	100 (80%)	10.6	96	10.4	8.4	-2
Torsion spring 3 (soft)	78 (62%)	9.4	78	9.4	7.7	-1.7

Table 4.2: Rigid mode

1st Elastic mode	**THEORETICAL**		**IMPLEMENTED**		**MEASURED**	**DIFFERENCE**
	Rot. Stiff. [Nm/rad]	**[Hz]**	**Rot. Stiff. [Nm/rad]**	**[Hz]**	**[Hz]**	**[Hz]**
Torsion spring 1 (hard)	126 (100%)	36.6	112	39.9	42.3	2.4
Torsion spring 2 (medium)	100 (80%)	42.6	96	43.4	42.9	-0.5
Torsion spring 3 (soft)	78 (62%)	46.9	78	46.9	44	-2.9

Table 4.3: First elastic mode

It can be seen from the results that the rigid modes are lower than expected. According to the analytical calculations, the elastic modes should then be found at higher frequencies than calculated for the implemented springs. This is indeed the case for TS1. However for TS2 and TS3 they are below the implemented values and more importantly not found at higher frequencies that correspond to the measured rigid modes.

To compare the behavior of the modes for the different torsion springs, these are plotted in the characteristic plot shown in figure 4.15. It is clear that the modes do follow the trend of the lines, but not accurately.
Due to the operational range of the shaker, the obtained values below 10 Hz do suffer from loss of accuracy. However, the values do decrease for lower rotational stiffness. Similar observations can be made for the elastic modes as these were expected to increase with lower stiffness. The deviated results can also be due to the noise level present in the system. During the experiments closer inspections in the frequency domain will be necessary.

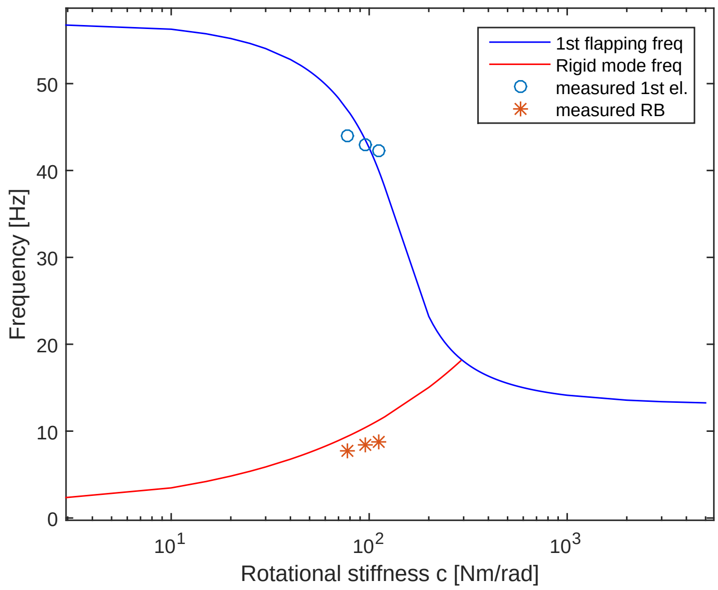

Figure 4.15: Measured modes in the characteristic plot (range 0-5000 Hz).

The blade was designed to have a rigid lagging mode at 3 Hz. Since the shakers have an operational range above 10 Hz, the blade is excited by an impact on the lag lever. The accelerometers are also placed in lagging direction at the same x-locations of the blade. The responses in frequency domain are shown in figure 4.16. It can be observed that the response in the middle and tip sensors have a high amplitude around 3 Hz. As the first accelerometer is found at the base, the acceleration there might not be as large as experienced by the others giving no clear peak. The rigid lagging mode is comparable to the oscillation frequency of a hanging pendulum. Due to the high inertia of the blade in lagging direction it is not expected to have elastic modes in this low frequency area, therefore the peak amplitude measured is justified to be the rigid mode.

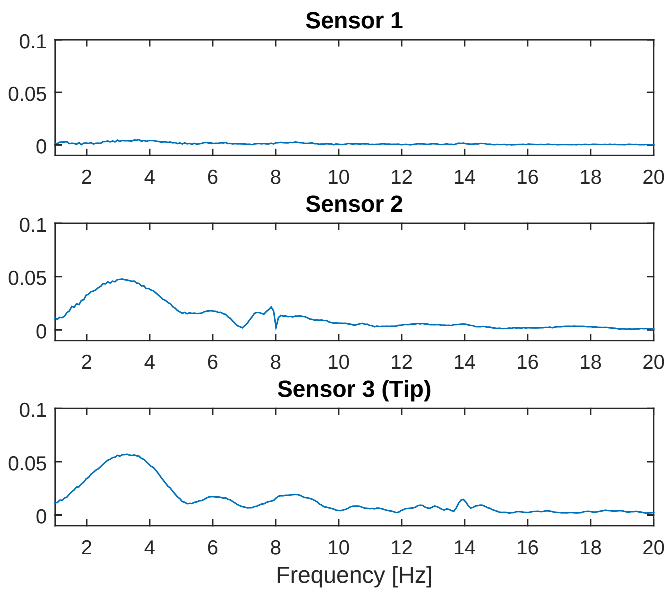

Figure 4.16: FFT of the lagging response.

4.3.3 Visualizing the blade response

A vibration shape can be defined whenever the vibration responses at two or more points on a surface with their directions (DOF) are measured. This is known as an Operating Deflection Shape (ODS) and illustrates the motion of a structure at a specific frequency or moment in time [16]. An ODS can be obtained from different types of time domain responses such as responses to random, impulsive or sinusoidal input signals. The ODS depends on the loads applied to the structure and changes when the loads do. If the structure's modes are changed, the ODS will also be different. Therefore a relation exists between the ODS and modeshapes that will be discussed later on. From the ODS will be clear how the loading on the blade changes the shape due to different operating conditions imposed on the demonstrator. ME'Scope will be used to obtain the deflection shapes from the experiments.

To verify the results, the modeshapes for TS1 from these frequencies have been plotted in figure 4.17, where clearly the differences between the rigid and elastic modes can be seen. This verification has also been done for the modes of the other torsion springs.

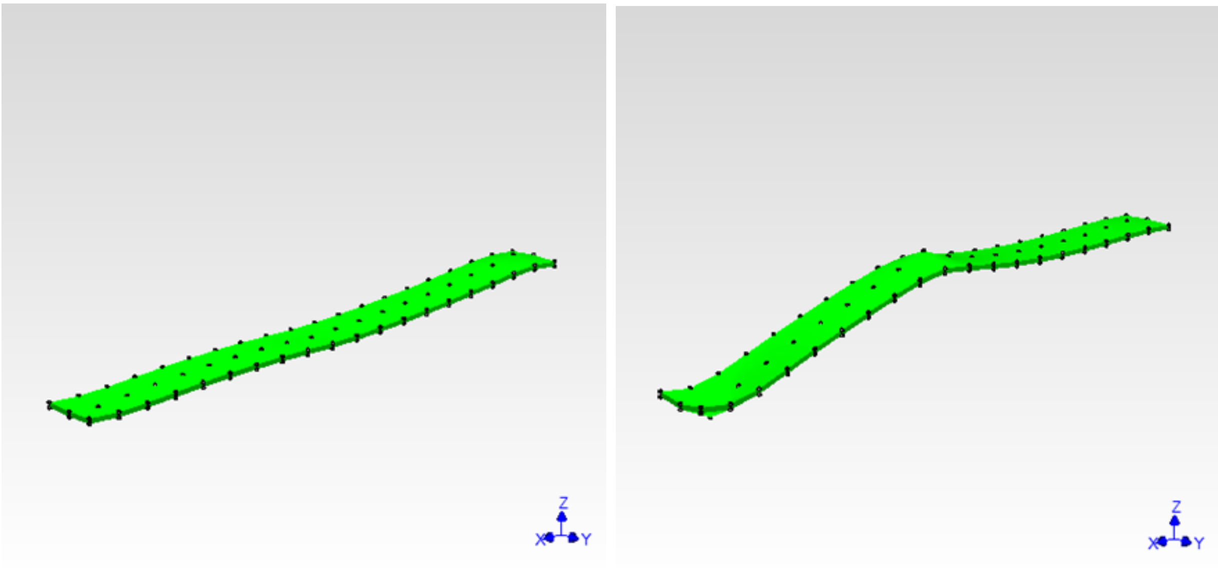

Figure 4.17: The modeshapes of the measured modes for TS1: (a) Rigid mode (b) Elastic mode

Chapter 5

Characterizing blade flapping

The flapping of the blade will be characterized by first performing an investigation of the simple flapping motion without operating effects. There after this motion will be influenced by exciting the lagging degree of freedom. The next inspection involves the more realistic flapping behavior i.e. harmonic distorted flapping. Blade lagging will again be applied and the effects on the response will be discussed. Lastly, the experiments will be repeated for the damage case to allow comparisons of the responses between the pristine and damaged blade.

The scheme in figure 5.1 illustrates the procedure for performing the experiments on the demonstrator. The analysis for TS1 will be discussed extensively and in the end evaluated with results from the other torsion springs. The baseline for flapping motion involves an excitation with a simple sinusoidal signal. The experiments then continue by applying influences of lagging on this base motion.

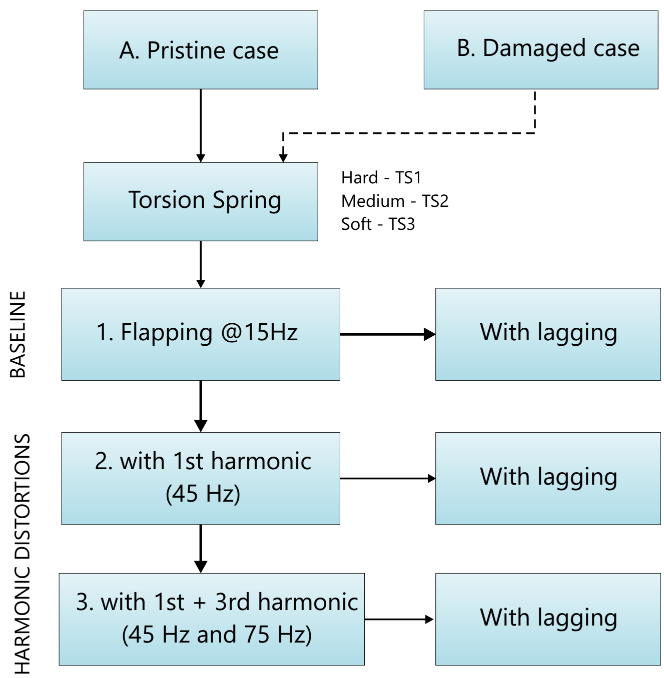

Figure 5.1: Experimental procedure for characterizing blade flapping in forward flight.

The loading in forward flight was already explained earlier and contains a series of uneven harmonics of the baseline frequency. These higher harmonics are characteristic indicators the system's response is nonlinear. The first uneven harmonic is at 45 Hz and the second uneven harmonic at 75 Hz.

5.1 Pure flapping motion

Figure 5.2 shows the time waveform input of the shaker and responses of the accelerometers on the blade to a simple sinusoidal flapping signal with a frequency of 15 Hz for TS1. When observing the input signal, the exerted force seems fairly harmonic and sinusoidal. However, from the FFT of this signal can be seen that the signal contains a harmonic at 30 Hz. When looking at the response of the blade, the accelerometers don't show clear sinusoidal responses as well. In fact, the responses show some periodic motion that could be a modulation of different frequencies. The FFT of these responses show additional frequencies showing up at 30 and 45 Hz, which could be considered the harmonics of the base frequency. Noticeable is that the accelerometer at the root of the blade shows a smaller reaction to the excitation compared to the tip sensor.

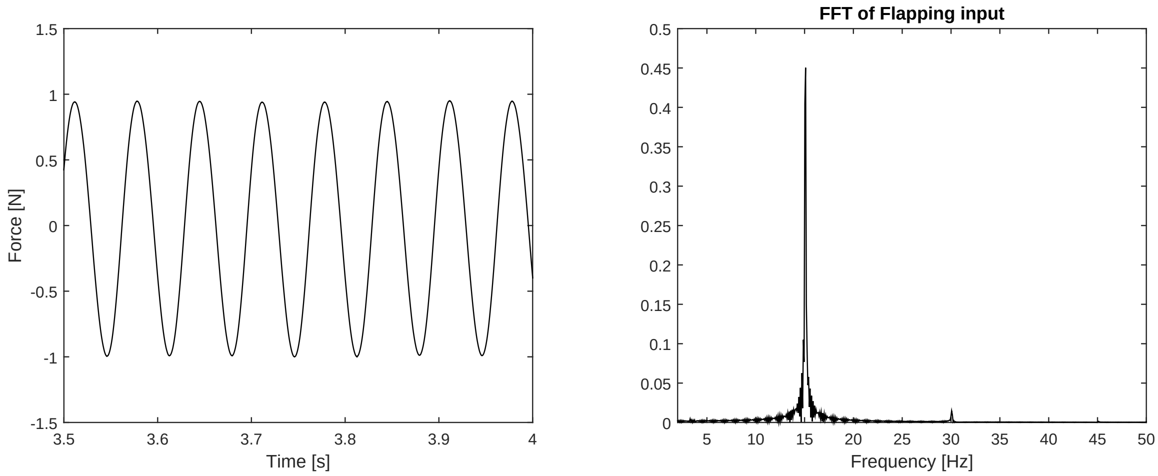

Figure 5.2: Shaker input force in (a) time domain and in (b) frequency domain.

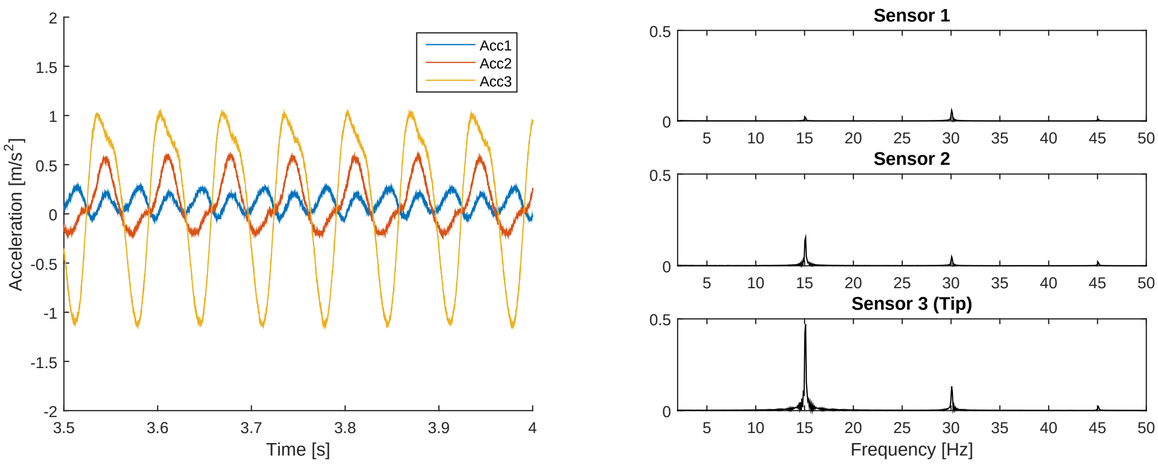

Figure 5.3: Blade response in (a) time domain and in (b) frequency domain.

A more efficient way of presenting the analyzed data, is in the form of a bar plot as illustrated in figure 5.4. The graph shows the amount of response for each encountered harmonic in the blade response. From this graph the earlier observation is verified that the tip of the blade responds the best to the excitation signal. The tip also shows the largest responses for the harmonics.
As the accelerometers are further away from the base, the responses to the excitation signals are more noticeable in the amplitudes. However, the base accelerometer shows a larger response than sensor 2 for the 30 Hz harmonic.

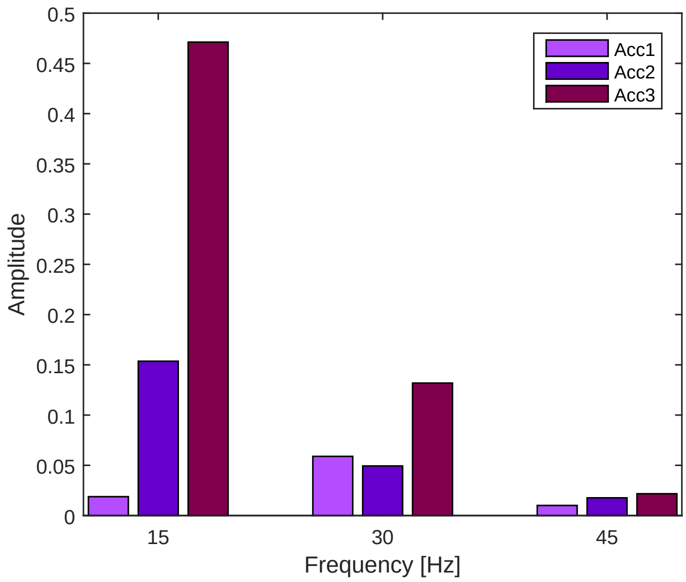

Figure 5.4: Amount of response at each accelerometer.

From the accelerometer data the operational deflection shape (ODS) was constructed in ME'Scope (figure 5.5). The measured rigid mode for the blade with TS1 was found at 8.7 Hz and the 1st elastic mode at 42.3 Hz. Therefore the expectation for this 15 Hz sinusoidal is that the deflection shape consists of a combination of these modes that is more towards the rigid mode. From the ODS can be seen that there is indeed some flexibility in the deflection, but that the overall motion seems to have an almost rigid nature.

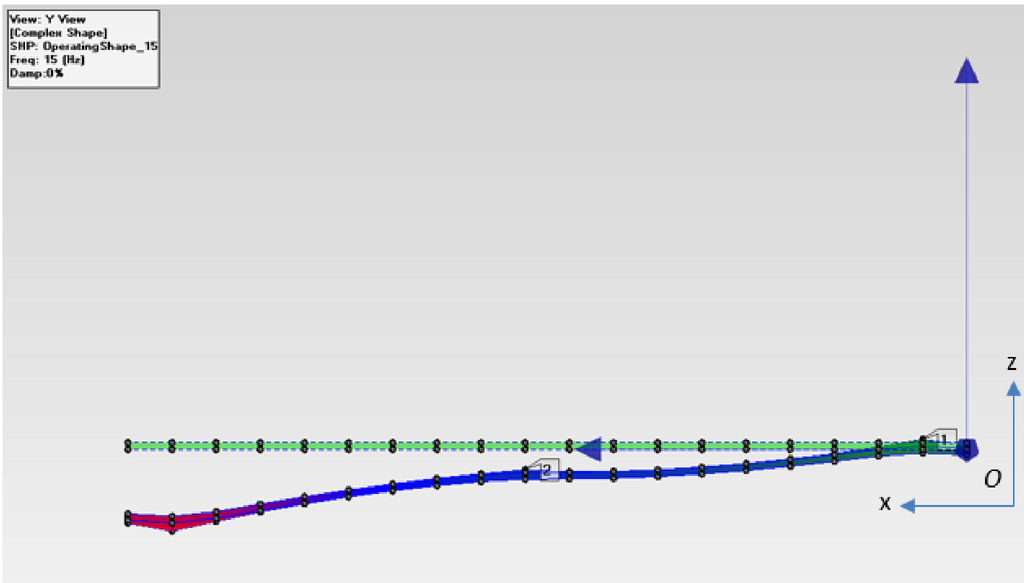

Figure 5.5: ODS in MEScope for blade flapping at 15 Hz.

5.1.1 Lagging influences

The next experiment involves lagging influences on the base flapping motion. By exciting the lagging degree of freedom with a sinusoidal signal at the same frequency of flapping, it is then presumed that lagging happens instantly as a consequence of flapping. In other words, lagging delays caused by e.g. the lag damper in a helicopter will not be considered for these experiments.

In figure 5.6 can be seen that due to low lagging input, the response in the blade accelerometers is noticeable more distorted than simple flapping. The FFT shows indeed additional responses for the 30 Hz and 45 Hz harmonic. The bar plot in figure 5.7b shows the differences with the simple flapping behavior. The negative values indicate a loss of response compared to simple flapping. The 15 Hz tip response is reduced by 10%. The 45 Hz harmonic response is between 100-170% higher in all three measurement points of the blade, indicating a sensitivity to this frequency throughout the blade. The reduction of the 30 Hz harmonic is in the order of 14-16%. Overall two things are important to gather from this plot: First of, the tip response to the excitation signal is reduced slightly due to lagging influences. Secondly, lagging introduces a much higher response for the 45 Hz harmonics and lower 30 Hz responses.

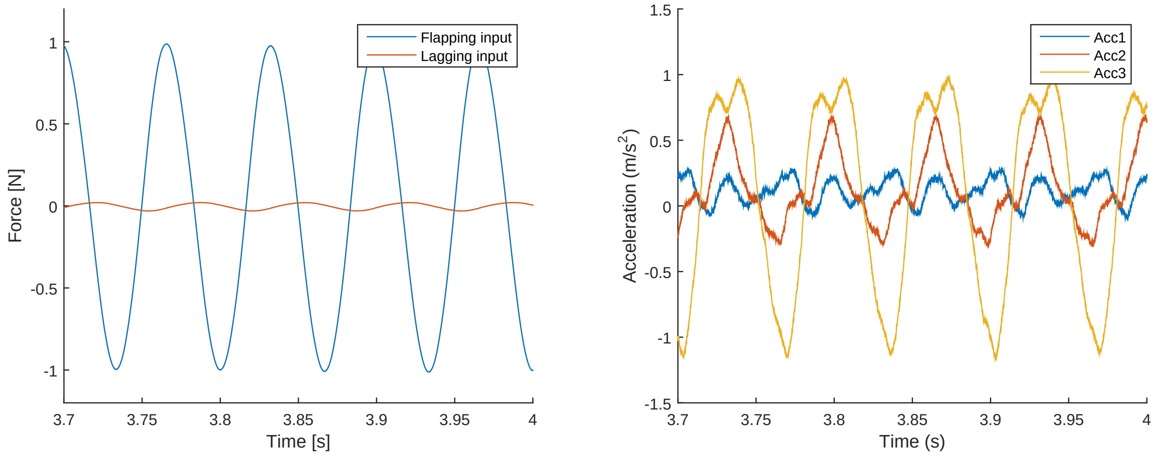

Figure 5.6: (a) Flapping and low lagging input forces. (b) Blade response.

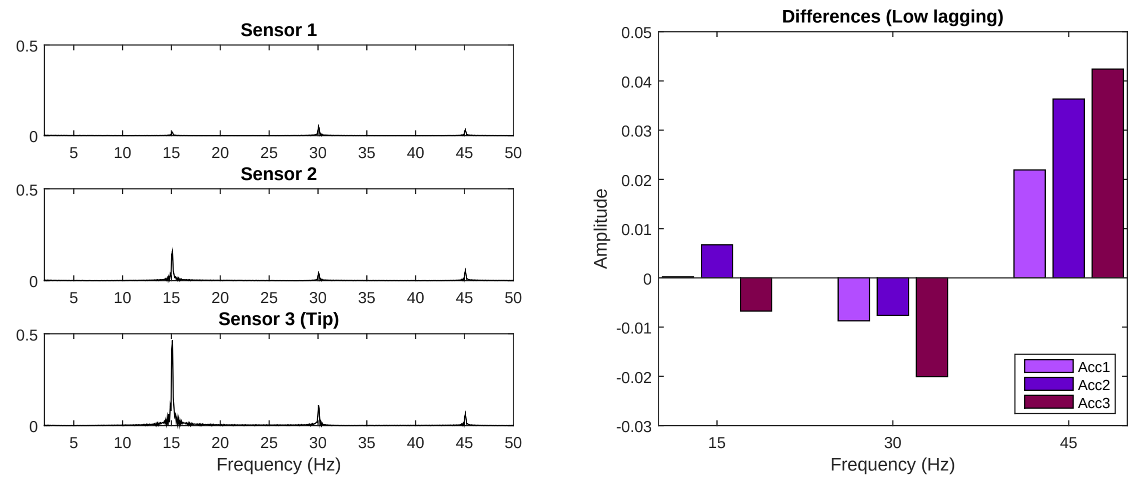

Figure 5.7: (a) FFT blade response to low gain lagging. (b) Differences with pure flapping.

5.1.2 Rotational stiffness variations

The analyses in the previous section have been done for TS1, indicating that the tip response contains the largest responses to excitations. For configurations with the other torsion springs, the analyses are done in a similar way and tip responses are plotted in figure 5.8.

From figure 5.8a can be seen that when the stiffness of the torsion springs decreases, the response amplitudes of the 15 Hz frequency also decrease by approximately 10%. However, the blade then becomes more sensitive for the 45 Hz harmonic. From table 4.3 can be seen that TS3 has a first elastic mode at 44 Hz, which is closer to 45 Hz harmonic compared to the modes of the other torsion springs. Therefor it can be stated that at lower rotational stiffness of the torsion springs, the rigid and first elastic modes of the blade diverge from each other causing less participation of the rigid mode in the response and leaving the blade prone to influences of higher harmonics. In the previous statement the observation is ofcourse only valid when the chosen excitation signal is in between the before mentioned modes.

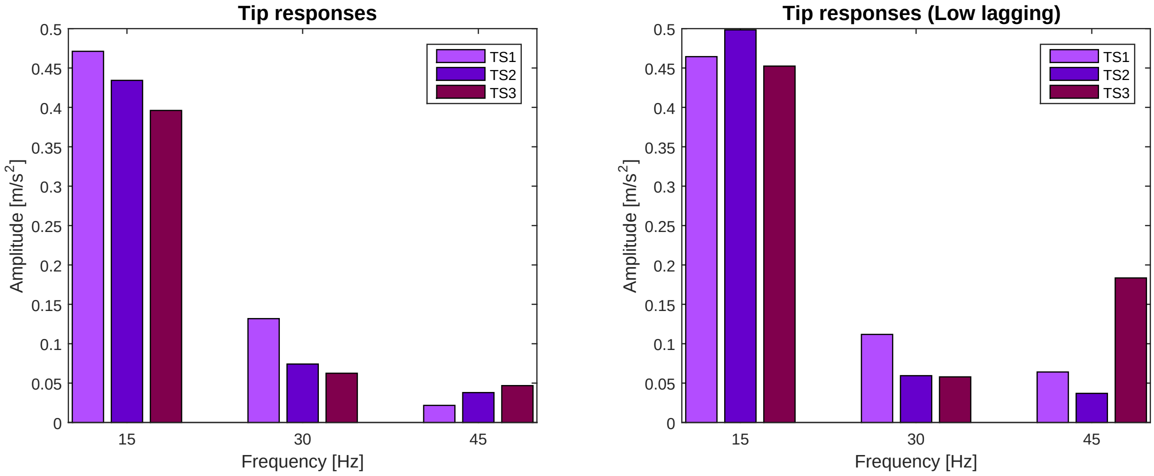

Figure 5.8: Tip responses to (a) simple flapping and (b) to flapping with lagging influences.

Considering now the influence of lagging on the flapping response of the blade, figure 5.8b shows that the tip responses to the 15 Hz increase for TS2 and TS3 in contrary to the previous findings for TS1.
With TS3's higher response of 15 Hz signal, also a clear increase of the 45 Hz harmonic can be observed. This suggests that the modal participation in the both responses has increased. A possible explanation to this scenario is that lagging increased both the rigid and first elastic mode of the blade, causing the harmonics to hit these resonance modes. The 30 Hz response remains approximately the same, therefore verifying that the elastic mode was not decreased.

Closer inspections in the frequency domain

The measurements have also been plotted in a logarithmic scale which are shown in appendix **??**. This allows a larger range of data to be displayed without compressing the small values at each frequency. From these plots it can be seen that more harmonics than the ones discussed above are present at higher frequencies. The influences of the lagging motion on the flapping input can also be seen more clearly.
The FFTs of simple flapping show that as the rotational stiffness of the torsion springs decreases, the flapping input is likely to suffer from higher harmonics. Figure 5.11 shows these harmonics and it can be observed that they are more in the higher frequency range. An interesting finding is that when lagging is introduced, the TS2 system contained more harmonics than TS3.

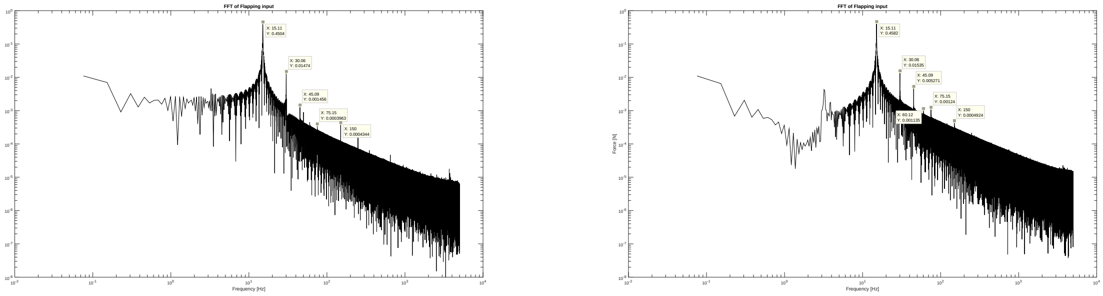

Figure 5.9: (a) Flapping input for TS1 showing the amount of harmonics in the system. (b) Flapping input with lagging for TS1.

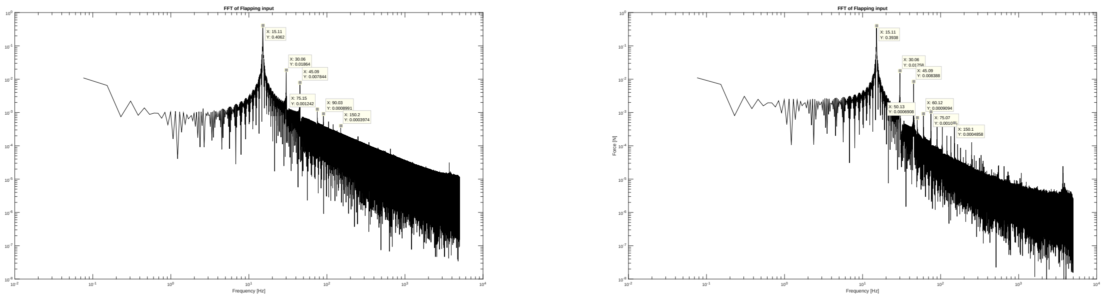

Figure 5.10: (a) Flapping input for TS2 showing the amount of harmonics in the system. (b) Flapping input with lagging for TS2.

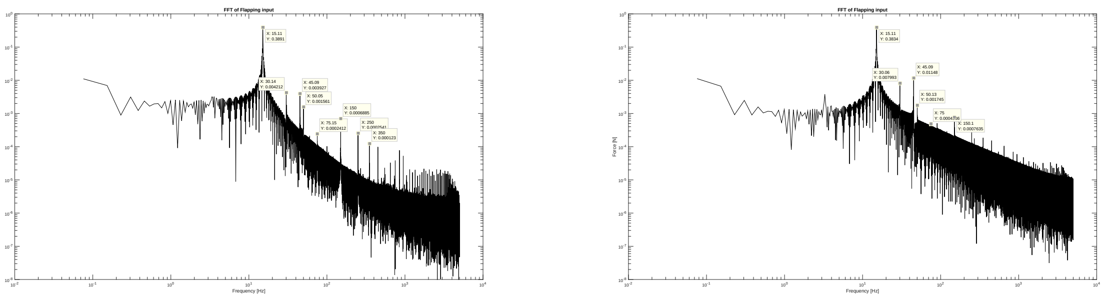

Figure 5.11: (a) Flapping input for TS3 showing the amount of harmonics in the system. (b) Flapping input with lagging for TS3.

5.2 Harmonic distorted flapping

The previous analyses will again be performed for the more realistic harmonic distorted flapping. The first odd harmonic of the baseline frequency and subsequently the second odd harmonic will be added to the flapping excitation where after these signals will again be influenced by lagging.

5.2.1 Distorted flapping

The input signal with only the baseline frequency and 45 Hz harmonic, will hereafter be mentioned as HD1. The second case, with both 45 and 75 Hz harmonic, will be HD2. Although the input signal was designed to be truncated in its maximum points, the force input plot in figure 5.12a shows the sinusoid to be dull

instead of flat in the peaks compared to simple flapping. The responses do seem to have less noise in the peaks.
In the frequency domain, figure 5.13 shows the sensitivity of the blade to the 45 Hz in the input signal as all three measurement points contain peaks close to or larger than amplitudes found at the baseline frequency. When comparing input and outputs it is clear that the 45 Hz response in the blade is amplified. If this is the cause of resonance due to the nearby elastic mode, will only be clear when the torsion springs are compared with each other. This will be investigated in the next part.

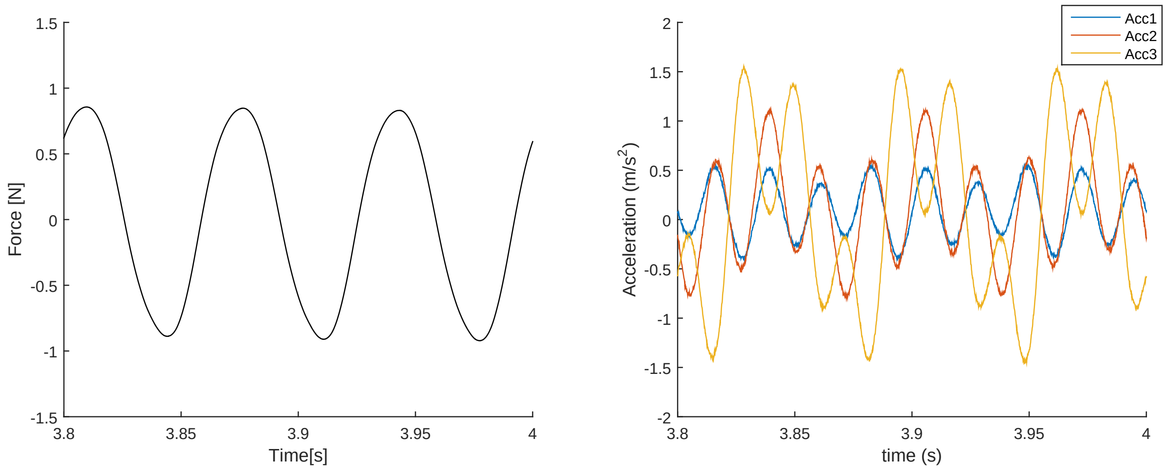

Figure 5.12: (a) Harmonic distorted flapping input with 1 harmonic. (b) Blade response to first harmonic.

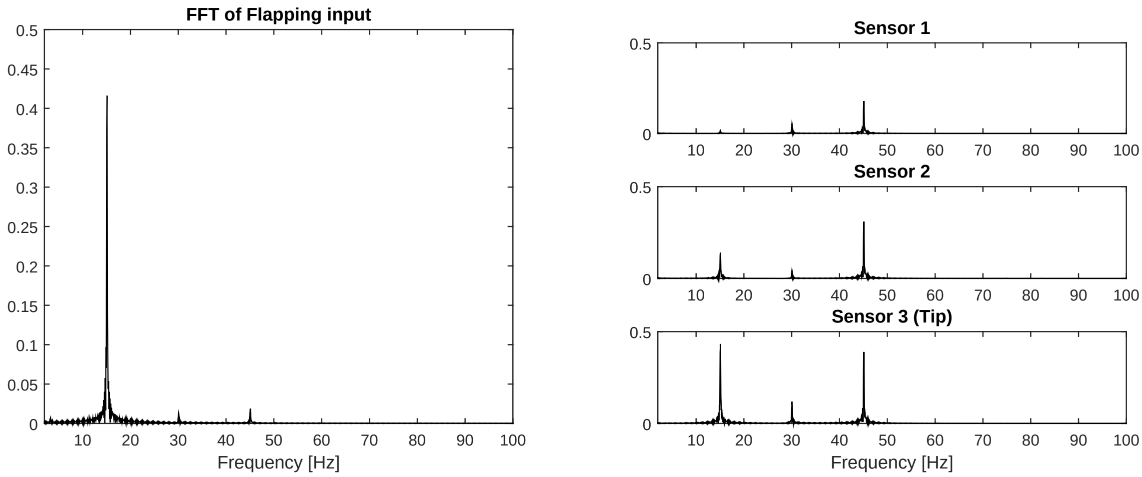

Figure 5.13: (a) Harmonic distorted input with 1 harmonic (HD1) (b) Response to HD1 case.

For the second case (HD2), with a harmonic at 75 Hz, the FFT of the input signal shows just a small peak at this frequency (fig. 5.14). In the response plot this indeed shows up in the blade, but is again very small compared to the former uneven harmonic. Therefore the addition of this harmonic has no significant effects in the response.

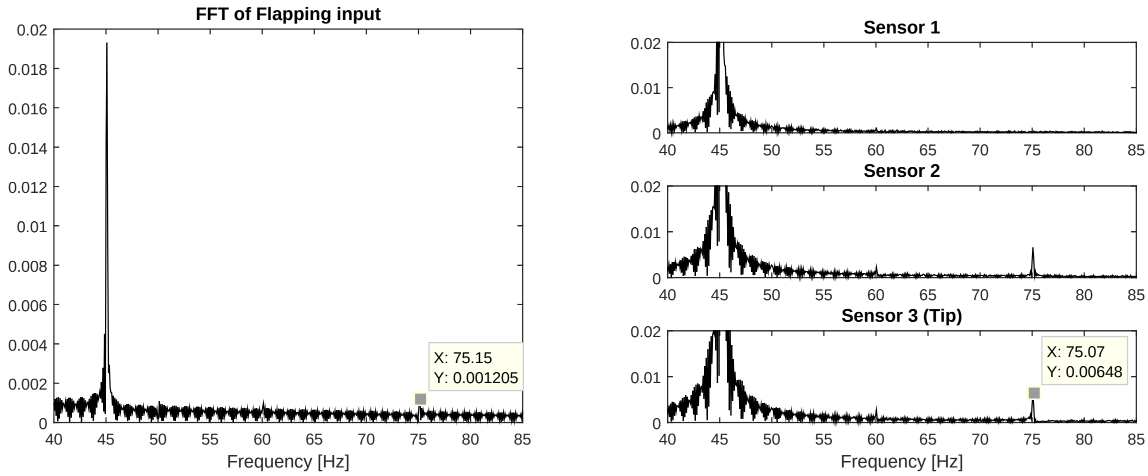

Figure 5.14: (a) Harmonic distorted flapping input with 2 harmonics (HD2). (b) Response to HD2 case.

5.2.2 Varying rotational stiffness

The bar plots in figure 5.15 show the difference in amplitude responses between HD1 and simple flapping for the different torsion springs. As expected, the 45 Hz responses have larger contributions in the HD1 response. With the exception of TS3, it can be seen that for lower torsion spring stiffness, the 45 Hz responses amplifies and therefor confirming that the nearby elastic mode of the blade is causing the resonance. From the observation that the 15 and 30 Hz responses in the whole blade are reduced at each configuration, confirms this.

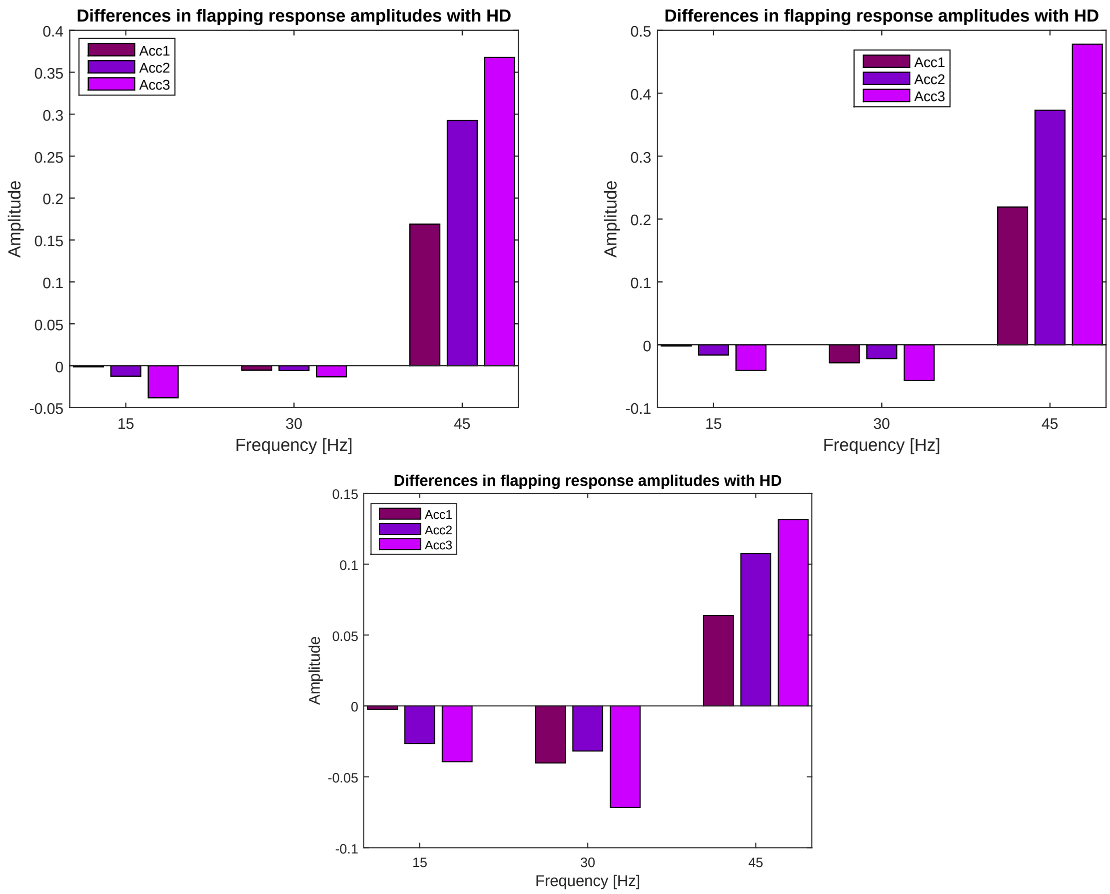

Figure 5.15: Differences compared to simple flapping for TS1, TS2 and TS3.

The peculiar result for TS3 requires the inspection of the whole FFT of the input and output signals. From figure 5.16, it can be seen that the 45 Hz response is indeed amplified compared to the input frequency. The reason why the difference between the simple flapping case is smaller compared to the other torsion springs then requires additional measurements and testing to find the root cause.

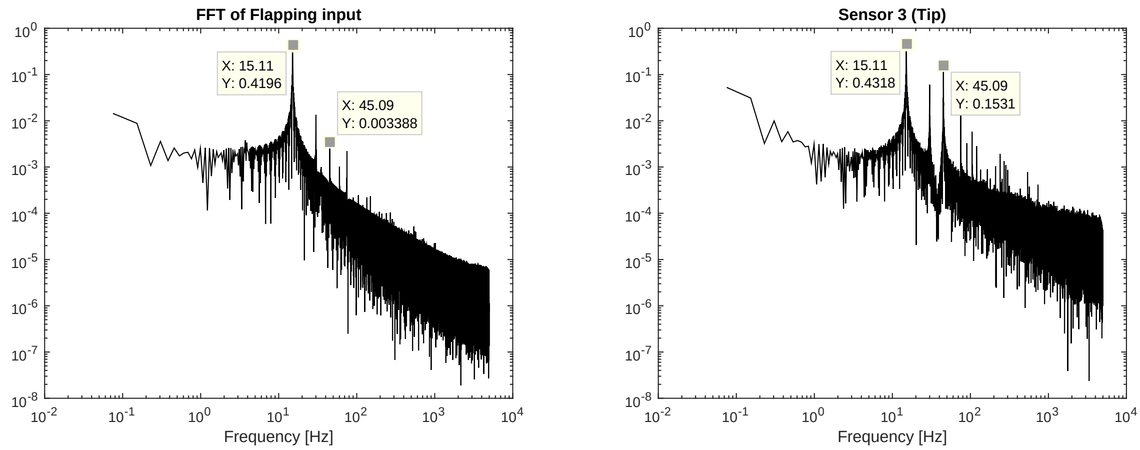

Figure 5.16: (a) HD1 flapping input and tip output for TS3.

5.2.3 Distorted flapping with low lagging

The bar plot in figure 5.17 shows the differences in response between HD1 and HD1 with lagging. With the exception of the 15 Hz response of the middle sensor, the amplitudes for the other frequencies are reduced with lagging. The tip has the largest differences with HD1 of which the 45 Hz is affected the most. However, notice that the differences are very small in magnitudes and differ at most 8% with HD1 responses. A better visual is required to conclude the findings, therefore figure 5.18 shows the measurements in the logarithmic scale. It can be seen that, although the bar plots show lower magnitudes for the two harmonics, the FFTs show increases for other higher harmonics. The noise level seems to be increased as well. As it is clear that lagging introduces more higher harmonics in this case, therefore the nonlinearity of the system increases.

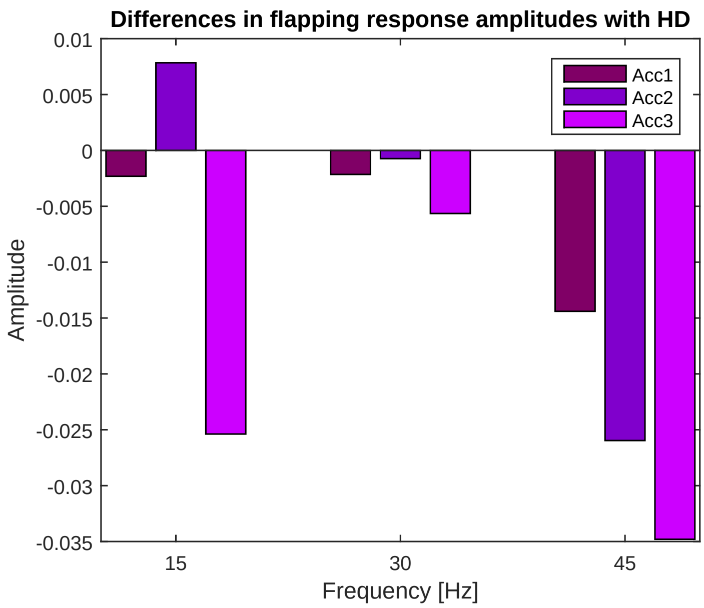

Figure 5.17: Differences between HD1 flapping and HD1 flapping and lagging.

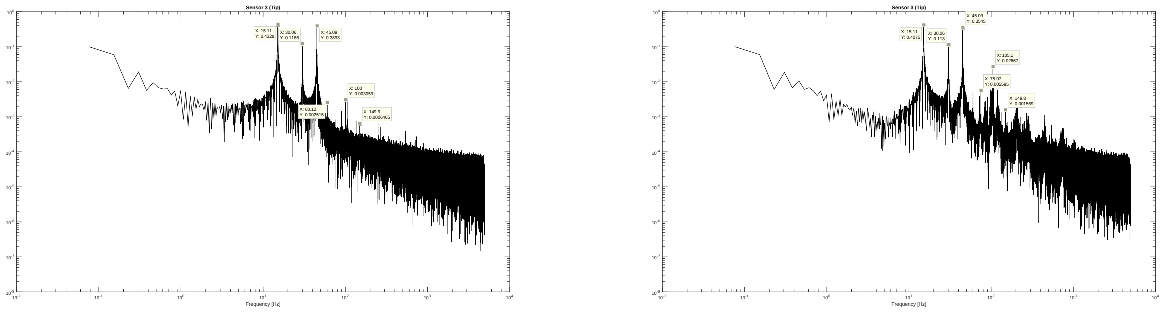

Figure 5.18: The tip accelerometer response to distorted flapping (HD1) compared to tip response to flapping (HD1) with influences of lagging.

HD2 will now be investigated with lagging influences. The bar plot shows a slight increase of responses in the 30 Hz harmonics, but all difference remain again under 8 %. From the FFTs no noticeable differences can be seen from the HD1 case. It can be concluded that either the extra harmonic in the input signal does not make a significant difference in the output for this case, especially with the noise content, or that the amount of Coriolis coupling might not be enough to induce more effects than found in the HD1 case.

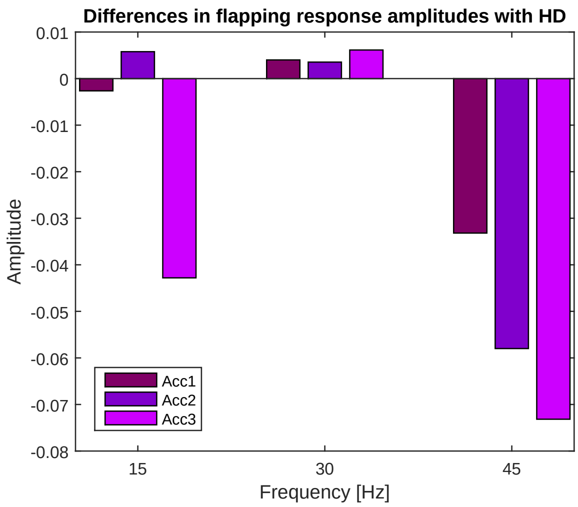

Figure 5.19: Differences between HD2 flapping and HD2 flapping and lagging.

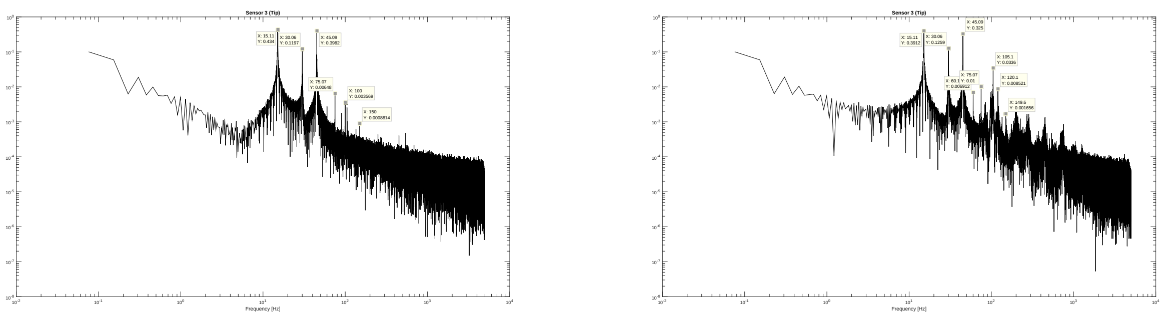

Figure 5.20: The tip accelerometer response to distorted flapping (HD2) compared to tip response to flapping (HD2) with influences of lagging.

5.3 The damage case

Damage results in mechanical degradation of the blade, resulting in a local reduction of bending stiffness. To perform this experiment, the damage scenario will however, be simulated by increasing the mass locally with a point mass. In this part the severity of damage will not be investigated, but the impact of an occurring damage on the previous blade responses for flapping.

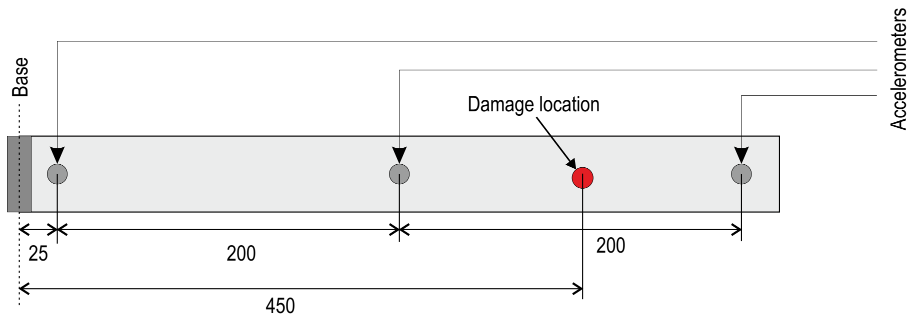

Figure 5.21: Blade scheme with damage.

5.3.1 Modal characterization

As the modal response of the blade is dependent on its stiffness properties, it is expected that damage decreases its natural frequencies with the added mass. To verify this modal analysis was performed to characterize the damaged blade. A comparison between the pristine and damage case is tabulated in table 5.1. With the exception of TS1, the other modes indeed show a decrease due to the damage.

	PRISTINE		**DAMAGED**	
	RB [Hz]	**1st Elastic [Hz]**	**RB [Hz]**	**1st Elastic [Hz]**
TS1 (hard)	8.7	42.3	6.9	44.7
TS2 (medium)	8.4	42.9	7.5	42.1
TS3 (soft)	7.7	44	7.4	43.7

Table 5.1: Modal parameters for the pristine and damage case of the blade.

5.3.2 Operational behavior

Simple flapping

From the input force plots in figure 5.22 there is no noticeable differences in amplitudes and frequencies, suggesting no feedback of the damaged blade on to the input signal that is different from the pristine case. The responses in the blade will then be completely due to the added-mass on the blade profile.

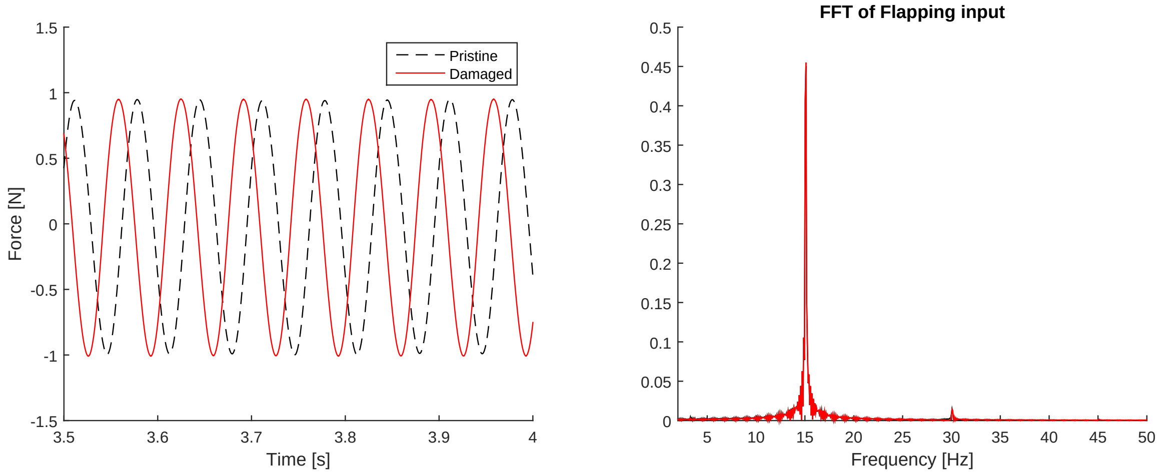

Figure 5.22: Shaker input force in the time and frequency domain.

Figure 5.23 presents the differences in responses between the pristine and damaged blade for only simple flapping. It can be seen that the 15 Hz responses for middle and tip sensors are reduced for the damaged case. The magnitudes for the other differences may be neglected due to the small values. From the FFTs of the tip responses in figure 5.25, it can be seen that higher harmonics occur. The 15 Hz response is thus reduced because of the increased vibrations in the blade.

When lagging is introduced in this case, it can be seen that the 30 Hz harmonic increases (figure 5.24). The decreased 45 Hz response might be ignored. Comparing the FFTs once more, shows even more vibrations occurring in the higher frequency range (figure 5.26).

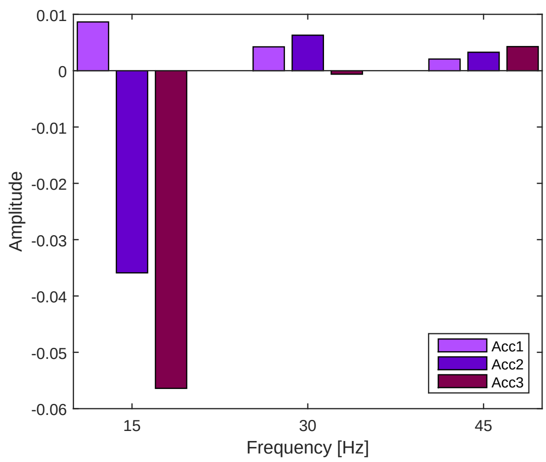

Figure 5.23: Response differences between damaged flapping and pristine simple flapping.

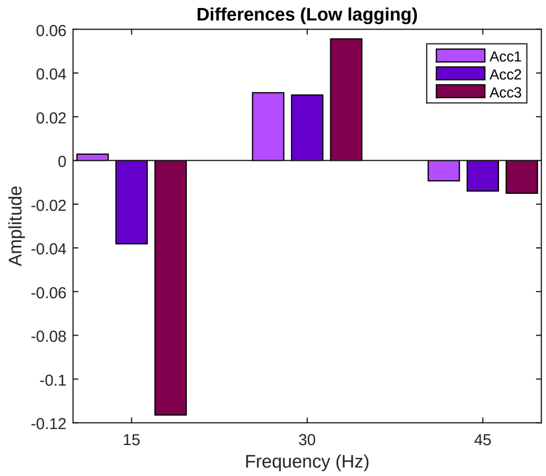

Figure 5.24: Response differences pristine flapping and flapping with lagging (damaged).

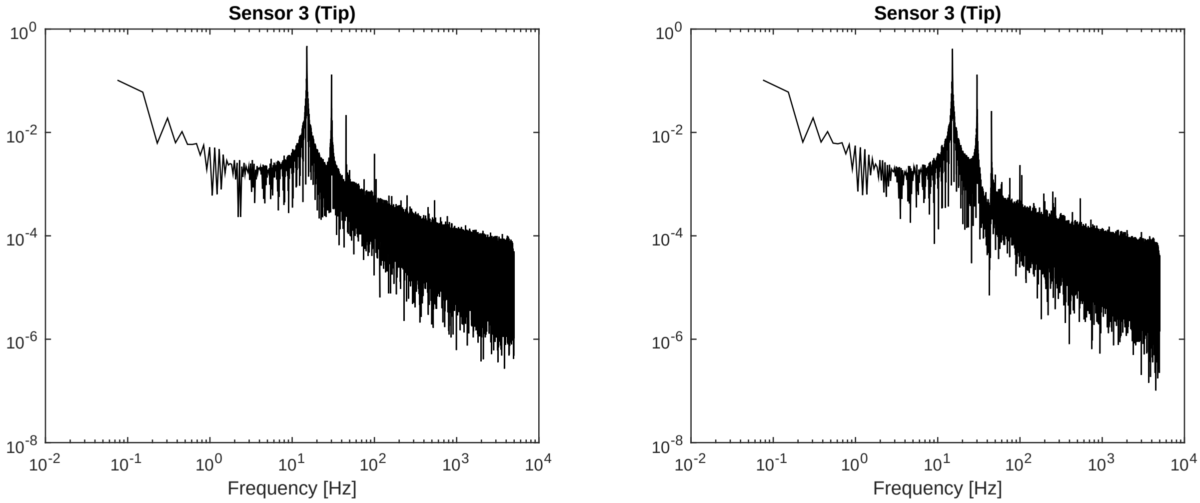

Figure 5.25: FFT of flapping for (a) pristine and (b) damaged blade.

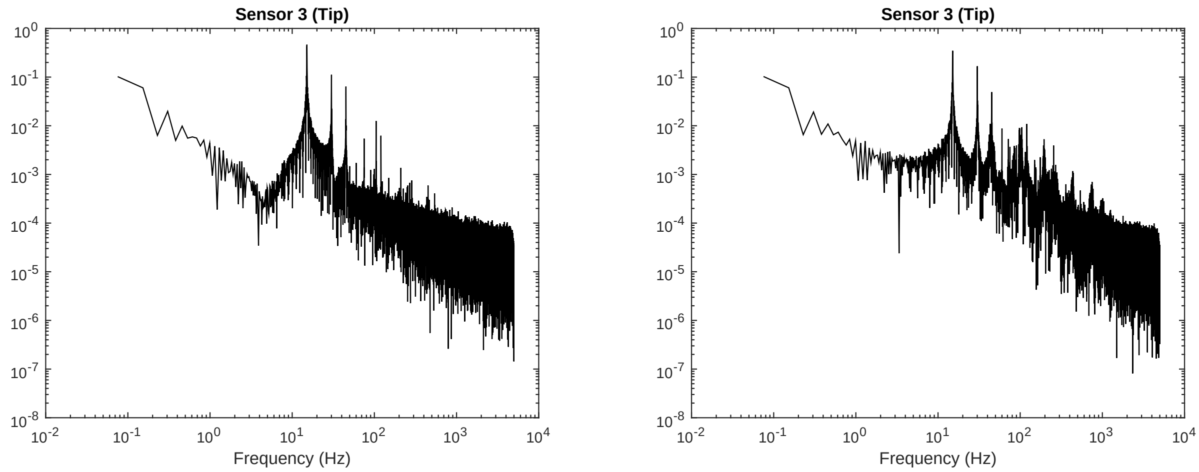

Figure 5.26: FFT of flapping with lagging for (a) pristine and (b) damaged blade.

Chapter 6

Conclusions and Recommendations

This research contributes to the experimental investigations of vibrations in a rotor blade by means of a demonstrator. Experiments were performed on a RBS demonstrator for configurations that represents flight conditions found in the forward flight of a helicopter. This chapter presents first the conclusions with respect to the operations of the demonstrator and finally the implications of the results for the helicopter case.

6.1 Conclusions

From the introduction was clear that the forward flight configuration requires a vertical thrust to move upwards and maintain altitude and a forward propulsive force to move in horizontal direction. With this forward motion the axisymmetry of wind flow through the rotor system is lost and therefore the blades experience non-stationary loading. As loading is dependent on the relative airflow through the blades, this means that the loading changes with position of the blade for each moment in the rotation. It could be seen that the relative velocities of wind experienced by a blade are then a function of the azimuth angle, which causes the flapping motion of the blade to perform in a harmonic distorted way.

This non-constant cyclic loading of the blade allows the existing phenomenas in rotating blades to respond in a way that is different from hovering. The Coriolis coupling, stress stiffening and aeroelasticity are affected by this, but also has relations with the flexibility of the blade that causes the blade to behave differently. The research question is therefore formulated as:

- *How can the blade responses to cyclic loading of the environment be represented in the existing demonstrator?*

The RBS demonstrator consists of a non-rotating blade that allows flapping, lagging and pitching motions. The coupling of lagging to flapping, the dissymmetry of lift and harmonic response of the flexible blades were interesting phenomena to be translated into appropriate excitations and constraints (boundary conditions) on the existing demonstrator.

A. Experiments on the demonstrator

The investigations on the current setup now involves the control of the boundary with rotational stiffness, which can provide different ratios of rigid and first elastic modes of the blade. Being able to control the ratio of these modes allows a variation of stiffness distribution throughout the blade.

With the investigation of the Coriolis coupling an extra degree of freedom was required to be excited, the lagging DOF. With this additional excitation the investigations on the demonstrator have been expanded from a 1 DOF to a 2 DOF system.

The occurrence of distortions in the lagging excitations for a too high gain of the amplifier, imposed limitations to the maximum moments that could be applied for blade lagging. The flapping moment was then lowered to the minimum, until the occurring harmonics in the input signal was still acceptable. With these two excitations tuned to their limits, the realizable Coriolis coupling was one with a lagging-flapping moment ratio of 0.2.

Influences of lagging on flapping

As expected, the simple flapping response of the blade revealed that the tip showed the highest responses to the excitation signal. As lagging is introduced to TS1 flapping, tip responses reduced slightly for the baseline frequency, 15 Hz and also for the 30 Hz harmonic. However, the amplitudes of the 45 Hz harmonics increased by approximately 100-170%.

As the tip of the blade was most sensitive to the excitation frequencies, it was also used to compare the responses of the flapping blade to the different torsion springs. The experiments then showed that as the rotational stiffness decreased, lower 15 Hz amplitudes were seen but increases of the 45 Hz responses (figure 5.8).
As lagging was then introduced to each of these systems, the TS2 showed higher tip responses for 15 Hz. The 45 Hz response was then noticeably lower than the other systems. A possible explanation suggested that lagging shifted the rigid and elastic mode frequency of the blade upwards, near the harmonics, so that the modal responses at 15 and 45 Hz increased. The 30 Hz response remained approximately the same, therefore verifying that the elastic mode was not decreased.

The distorted harmonic flapping

Two types of harmonic distorted input signals were used to resemble the more realistic flapping of the rotor blade. The first signal included the 3rd harmonic, so at 45 Hz. The second signal included the 3rd and 5th harmonic, i.e. 45 and 75 Hz.
The results showed that the 45 Hz harmonic was amplified compared to the simple flapping. As the blade contains its elastic mode near this harmonic, it is justified to say that the extra harmonic in this input signal caused the higher modal response in the blade for 45 Hz. For decreasing rotational stiffness, the elastic mode comes closer to the 45 Hz harmonic, therefore the amplification is larger. This was evident from the bar and FFT plots.
Furthermore, from the responses it could be concluded that the effects of the 5th harmonic were not significant enough to make a difference in the flapping blade response compared to the 45 Hz. Reason for this might be the low amplitude of this harmonic in the input signal with the presence of noise.

Damaged case

For this case a point mass was fixed on the blade that simulated a case similar to damage as a result of local reduction of bending stiffness. Expected is that increased vibrations can be an indication that a failure process is taking place. Therefore the severity of damage was not important for this test, but merely the effects on the previous analyses.
The modal analyses revealed that the rigid and elastic modes more or less decreased with the added mass. From the operational behavior, it could also be seen that the 15 Hz response showed reduced amplitudes, but the amount of higher harmonics in the response increased. With the addition of lagging, the amount increased even more.

B. Implications for vibration monitoring

The experiments on the demonstrator showed how sensitive the blade reacted to the excitation frequency.

Monitoring of vibrations on the helicopter blade then proves to be a complex task for the different phenomena encountered in forward flight.
The rotational stiffness determines the stiffness throughout the blade, which is similar to the coning characteristic of the helicopter. Cyclic changes of the loading in forward flight results in a variation of this coning, hence a variation in stiffness distribution. From the different torsion spring analyses it could be seen that when the blade then has a structural mode at a harmonic of the excitation frequency, the responses at and near that frequency, amplifies.

The experiments showed that lagging influences the flapping motion by reducing its baseline frequency amplitude. The 3rd harmonic increases, however. This implies that the Coriolis coupling results in higher harmonics throughout the blade. With these higher harmonics less rigid behavior is found in the blade's motion, leaving the blade more prone to aeroelastic effects.
In the rotating blade it was known that the eigenfrequencies are a combination of structural properties and stress stiffening effects. Applying a lagging motion to the non-rotating blade while flapping might show similar effects on the modes. For the TS2 case it could be seen that the 15 Hz response increased while the 45 Hz decreased. This indicated a higher modal response of the rigid mode and therefore an example of how lagging can influence the modes.
As damage was introduced in the system, it was quickly seen that the baseline frequency responses reduced slightly, but that the higher frequency vibrations increased. As was already clear from the pristine cases, the system is sensitive to the higher harmonics. A clear boundary between the pristine flapping and damaged flapping was hard to determine without additional tests.

6.2 Recommendations

The experiments performed on the demonstrator can be improved for situations where more accuracy was required to form appropriate conclusions. The anomalies in the measurements could be either due to the sensor system, actuators or the geometrical non-linearities of the demonstrator itself. These are discussed next.

- The blade responses to the different excitations were measured with three accelerometers. After interpolating between these measurement points, the deflection shapes were somewhat questionable with respect to the amount of bending of the sections of the blade. As each point has the possibility to be an outlier in a series of measurements, increasing the amount of measuring points improves the statistics for achieving a better shape. A laser vibrometer might be a suitable alternative. The characterization of the lower modes of the blade could also be estimated more accurately.

- The measurement results revealed a lot of harmonics present in input signal of the system. It could be concluded that the shaker output is effected by the response of the demonstrator. The question remains if a shaker with more mass can resolve this problem. This needs to be investigated. As an alternative to compensate for the harmonics in the output signal of the shaker, an input signal could be designed that opposes the amplitudes of the harmonics. A pure flapping motion can then be achieved. The input signal would then have to be adjusted for each torsion spring configuration as the feedback on the shaker might then be different.

Due to the problems in the setup, more time and testing was required to fully characterize the behavior of the blade. Subsequently, the characterization of the blade response to the cyclic loading had to account for the occurring harmonics and noise in the demonstrator. Establishing a boundary as mentioned in figure 1.3 was hard to realize due to the uncertainties. The results presented in this thesis are part of a qualitative analyses. The observations can be validated with the help of the deflection shapes of the blade. In a quantitative way, these deflection shapes should be a combination of the determined rigid and elastic modes. It is recommended as a next step to perform this analyses after the inaccuracies of the measurements are solved.

References

[1] A. Bramwell, G. Done, and D. Balmford. Bramwell's Helicopter Dynamics. *Bramwell's Helicopter Dynamics*, pages 33–76, 2000.

[2] Civil Aviation Authority. HUMS Extension to Rotor Health Monitoring. Technical report, CAA, 2008.

[3] T. Dahlberg. The Effect of Modal Coupling in Random Vibration Analysis. *Journal of Sound and Vibration*, 228(1):157–176, 1999.

[4] P. H. de Jong. *Power Harvesting using Piezoelectric Materials*. 2013.

[5] R. C. F. G. *Operational Modal Analysis of Civil Engineering Structures*. 2014.

[6] G.Leishman. *Principles of helicopter aerodynamics*. 2006.

[7] J. Holman. *Experimental methods for engineers*, volume 9. 1994.

[8] L. Meirovitch. Fundamentals of Vibrations, 2001.

[9] K. Q. Nguyen. Higher Harmonic Control Analysis for Vibration Reduction of Helicopter Rotor Systems. (October 1994), 1994.

[10] T. H. Ooijevaar. *Vibration based structural health monitoring of composite skin-stiffener structures*. 2014.

[11] S. Oosterik. Towards on-blade monitoring of rotating blade systems. 2014.

[12] P. Pawar and R. Ganguli. Helicopter rotor health monitoring- a review. *Proceedings of the Institution of Mechanical Engineers, Part G: Journal of Aerospace Engineering*, 221(OCTOBER 2007):631–647, 2007.

[13] A. S. Ramirez, R. Loendersloot, and T. Tinga. Helicopter Rotor Blade Monitoring using Autonomous Wireless Sensor Network. *Cm & Mfpt*, (3), 2013.

[14] S. S. Rao. *Mechanical Vibrations - Chapter 13*. 1995.

[15] S. S. Rao. *Mechanical Vibrations*. 2011.

[16] M. H. Richardson. Structural Dynamics Measurements Rules of Digital Measurement. pages 1–13, 1999.

[17] A. Sanchez, R. Loendersloot, and T. Tinga. A vibration monitoring system design framework based on understanding of damage and failure. pages 1–19, 2015.

[18] T. Sanchez, A; Loendersloot, R; Jauregui, J; Tinga. Design Framework for Vibration Monitoring Systems for Helicopter Rotor Blade Monitoring using Wireless Sensor Networks. 2013.

[19] A. Sanchez Ramirez, K. Das, R. Loendersloot, T. Tinga, and P. Havinga. Wireless Sensor Network for Helicopter Rotor Blade Vibration Monitoring: Requirements Definition and Technological Aspects. *Key Engineering Materials*, 569-570:775–782, 2013.

[20] S. T. Smith. *Flexures - Elements of Elastic Mechanisms*. Overseas Publishers Association N.V., 2000.

[21] H. Soemers. *Design Principles for precision mechanisms*. 2011.

[22] G. E. Teunis. Output-only Modal-based Structural Health Monitoring in composite beams. 2015.

[23] D. Wagg, S. Neild, C. W. S. To, and S. K. Lau. *Nonlinear Vibration with Control*, volume 58. 2010.

[24] J. Watkinson. *Art of helicopters*, volume 1.

[25] J. Wolters. Design and Construction of a Setup that Represents the Behavior of Helicopter Rotor Blade System. 2014.

Appendices

Appendix A

Blade modes

The elastic flapping frequencies can be found with:

$$\rho A \frac{\partial^2 w(x,t)}{\partial t^2} + EI \frac{\partial^4 w(x,t)}{\partial x^4} = 0 \tag{A.1}$$

The free vibration solution is found using the method of separation of variables:

$$w(x,t) = W(x)T(t) \qquad \text{(standing waves)} \tag{A.2}$$

Using above, leads to:

$$\rho AW(x) \frac{d^2 T(t)}{dt^2} + EIT(t) \frac{d^4 W(x)}{dx^4} = 0 \tag{A.3}$$

$$\Rightarrow \frac{1}{T(t)} \frac{d^2 T(t)}{dt^2} = -\frac{EI}{\rho AW(x)} \frac{d^4 W(x)}{dx^4} = \omega^2 \tag{A.4}$$

As we are only interested in the spatial solution, the right hand equations is thus:

$$-\frac{EI}{\rho AW(x)} \frac{d^4 W(x)}{dx^4} = \omega^2 \tag{A.5}$$

$$\Rightarrow \frac{d^4 W(x)}{dx^4} - \frac{\rho AW(x)}{EI} \omega^2 = 0 \tag{A.6}$$

$$\Rightarrow \frac{d^4 W(x)}{dx^4} - \beta \omega^2 = 0 \tag{A.7}$$

This is a 4^{th} order problem with $\beta = \frac{\rho AW(x)}{EI}$. The general solution of this problem is in the form:

$$Y(x) = B_1 cos(\beta x) + B_2 sin(\beta x) + B_3 cosh(\beta x) + B_4 sinh(\beta x) \tag{A.8}$$

To determine the constants, the following boundary conditions are considered:

At x = 0:

Zero displacement:
$$Y(0) = 0 \tag{A.9}$$

Zero bending, with torsional stiffness:
$$EI \frac{d^2 Y(x)}{dx^2} + c \frac{dY(x)}{dx} = 0 \tag{A.10}$$

At x = L:

Zero bending:
$$\frac{d^2 Y(x)}{dx^2} = 0 \tag{A.11}$$

Shear force:
$$\frac{d^3 Y(x)}{dx^3} = 0 \tag{A.12}$$

After substitution A.9 in the general solution, gives for the constants:

$$Y(0) = B_1 + B_3 = 0 \tag{A.13}$$
$$\Rightarrow B_1 = -B_3 \tag{A.14}$$

The solution then reads:

$$Y(x) = B_3(-cos(\beta x) + cosh(\beta x)) + B_2 sin(\beta x) + B_4 sinh(\beta x) \tag{A.15}$$

The first, second and third derivatives are required in the boundary conditions, so these are derived as follows:

$$\frac{dY(x)}{dx} = \beta B_3(sin(\beta x) + sinh(\beta x)) + \beta B_2 cos(\beta x) + \beta B_4 cosh(\beta x) \tag{A.16}$$
$$\frac{d^2Y(x)}{dx^2} = \beta^2 B_3(cos(\beta x) + cosh(\beta x)) - \beta^2 B_2 sin(\beta x) + \beta^2 B_4 sinh(\beta x) \tag{A.17}$$
$$\frac{d^3Y(x)}{dx^2} = \beta^3 B_3(-sin(\beta x) + sinh(\beta x)) - \beta^3 B_2 cos(\beta x) + \beta^3 B_4 cosh(\beta x) \tag{A.18}$$

This solution equation will now be evaluated at $x = 0$. Using boundary condition A.10 the solution equation gives:

$$EI(2\beta^2 B_3) + c\beta(B_2 + B_4) = 0 \tag{A.19}$$

Next, using the derivatives in A.11 and A.12 at $x = L$:

$$\beta^2 B_3(cos(\beta L) + cosh(\beta L)) - \beta^2 B_2 sin(\beta L) + \beta^2 B_4 sinh(\beta L) = 0 \tag{A.20}$$
$$\beta^3 B_3(-sin(\beta L) + sinh(\beta L)) - \beta^3 B_2 cos(\beta L) + \beta^3 B_4 cosh(\beta L) = 0 \tag{A.21}$$

As there are three unknowns and three equations, the system can be put into matrix-vector notation:

$$\begin{bmatrix} c\beta & 2EI\beta^2 & c\beta \\ -\beta^2 sin(\beta L) & \beta^2(cos(\beta L) + cosh(\beta L)) & \beta^2 sinh(\beta L) \\ -\beta^3 cos(\beta L) & \beta^3(-sin(\beta L) + sinh(\beta L)) & \beta^3 cosh(\beta L) \end{bmatrix} \begin{Bmatrix} B_2 \\ B_3 \\ B_4 \end{Bmatrix} = \begin{Bmatrix} 0 \\ 0 \\ 0 \end{Bmatrix} \tag{A.22}$$

The non-trivial solution is found from the characteristic equation, that is obtained when setting the determinant of the matrix to zero:

$$\begin{aligned} c.cos^2(\beta L) + c.cosh^2(\beta L) + c.sin^2(\beta L) - c.sinh^2(\beta L) + 2c.cos(\beta L)cosh(\beta L) \\ -2EI\beta cos(\beta L)sinh(\beta L) + 2EI\beta sin(\beta L)cosh(\beta L) = 0 \end{aligned} \tag{A.23}$$

The values of β are found by numerically finding the intersection with x-axis ($y = 0$) in Matlab after specifying the rotational stiffness. The eigenfrequencies of the system can then be found with:

$$\omega_n = (\beta L)^2 \sqrt{\frac{EI}{mL^3}} \tag{A.24}$$

Appendix B

Operational Deflection Shapes

The Operational Deflection Shapes of flapping compared with flapping and lagging for TS1.

Flapping

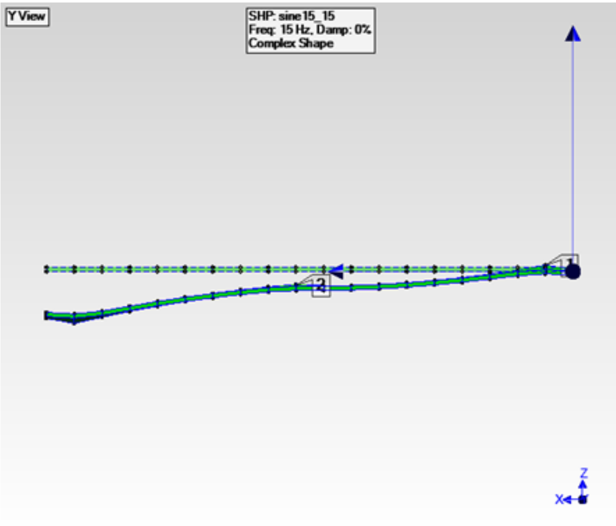

Figure B.1: ODS in MEScope for blade flapping at 15 Hz.

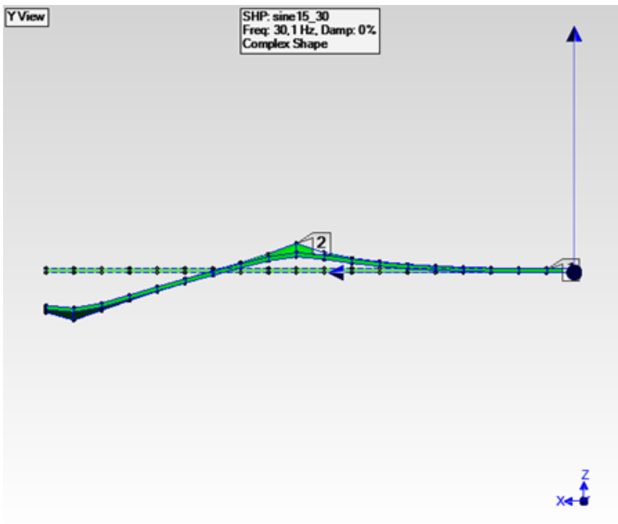

Figure B.2: ODS in MEScope for blade flapping at 30 Hz.

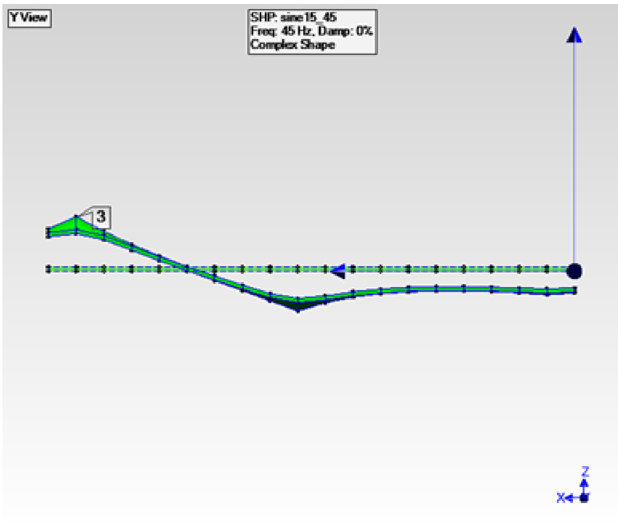

Figure B.3: ODS in MEScope for blade flapping at 45 Hz.

Flapping and lagging

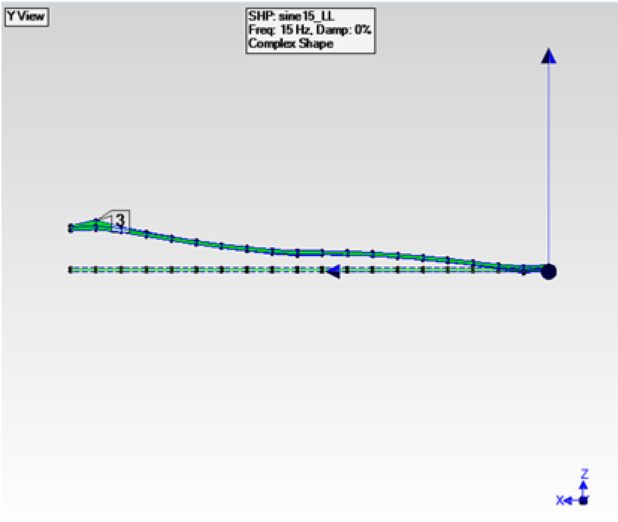

Figure B.4: ODS in MEScope for blade flapping and lagging at 15 Hz.

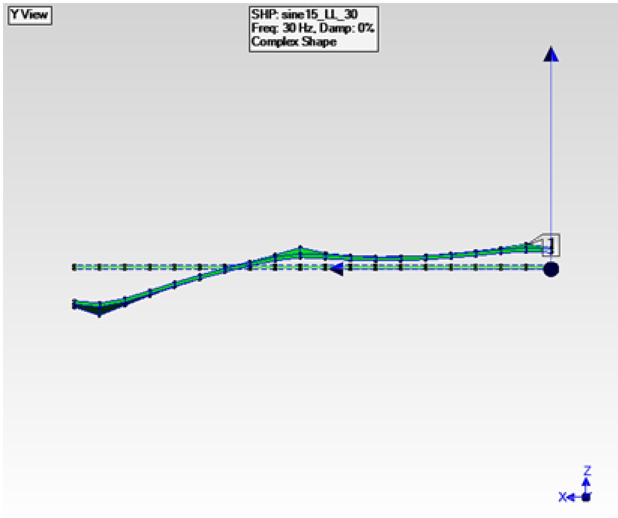

Figure B.5: ODS in MEScope for blade flapping and lagging at 30 Hz.

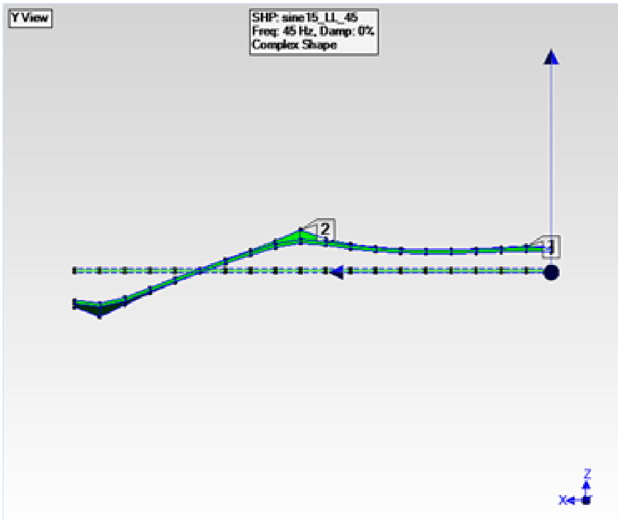

Figure B.6: ODS in MEScope for blade flapping and lagging at 45 Hz.